Volcano dynamics vs tectonics on Mars: evidence from Pavonis Mons

Riccardo Pozzobon[1], Diana Orlandi[2], Carolina Pagli[2], Francesco Mazzarini[3]

1) Dipartimento di Geoscienze, Università degli Studi di Padova

2) Dipartimento di Scienze della Terra, Università di Pisa

3) Istituto Nazionale di Geofisica e Vulcanologia, Pisa

Abstract

Volcanic activity is widespread within the inner Solar system and it can be commonly observed on rocky planets. In this work, we analyse the structures of Pavonis Mons in the Tharsis volcanic province of Mars by performing structural mapping, azimuth, and topographic distribution of linear features on the flanks of Pavonis, such as grabens and pit chains. We tested whether their formation is to be ascribed to the volcano dynamics and magmatic activity or the tectonics. Through the length size distribution and fractal clustering analyses of the structural features, we found that large grabens are vertically confined in the upper mechanical layers of the brittle crust whereas pit chains penetrate the whole crust up to the magmatic source, indicating that they can be considered the main feeders of Pavonis Mons. We inverted the topography with dykes and faults models to test whether grabens at the surface are the expression of intrusions at depth and we suggest that thin dykes inducing normal faulting are the most likely mechanism. Furthermore, two azimuthal distribution of the grabens are identified: concentric grabens occur on the volcano summit while linear grabens at its base show NE-SW trend as the Tharsis Mons volcanos alignment. The occurrence of linear grabens suggests that Pavonis likely experienced a phase of active rifting with the formation of such structures, followed by a phase of volcano growth and concentric magma intrusions when volcano and magma chamber dynamics prevailed.

1.0 Introduction

Planetary grabens, identified as linear topographic lows bordered by normal faults, have been widely recognized on Mars and other rocky planets as well as on the Moon (Ernst et al., 2003; Watters et al., 2012; Klimczak, 2014). However, the origin of these structures is debated (Mège et al., 2003). On Earth linear grabens may form due to dyke intrusions (Gudmundsson and Loetveit, 2005; Gudmundsson et al., 2008; Koehn et al., 2019; Wyrick and Smart, 2009), normal faulting (Melosh and Williams, 1989; Koehn et al., 2019) or a combination of both dyke-induced normal faulting above a dyke- (Gudmundsson and Loetveit, 2005) in extensional tectonic regimes (Mège et al., 2003; Acocella and Neri, 2009). Besides, concentric dykes can also originate from a pressurized magma chamber without any active tectonics (Acocella and Neri, 2009; Bistacchi et al., 2012) or, at the regional scale, they can be caused by interaction between magmatism and lithospheric flexure due to loading (Galgana et al., 2013; Grosfils et al., 2015). Therefore, both extensional tectonics and volcano dynamics can have played an important role in the formation of Mars grabens. The formation and evolution of the Tharsis volcanic province is still a matter of debate and several hypotheses have been suggested for the formation of such a huge volcanic province, including the presence of a plume on a stationary plate (Meyzen et al., 2014) or on a decoupled lithosphere-mantle with differential rotation (Zhong, 2008), a giant impact resulting in the formation of a large igneous province (Reese et al., 2004), episodic rollback of a subducting slab (Yin, 2012).

Here we explore whether volcano dynamics or tectonic processes control deformations at Pavonis Mons by analysing in detail i) the variation of graben azimuth distribution from its base to the summit, ii) the spatial clustering of grabens and pit chains in the volcano and iii) the volcano-tectonic structures on the volcano summit. We find that the azimuthal distribution of grabens shows two main patterns: concentric grabens occur on the volcano summit and linear grabens at its base. We interpret the linear grabens at the base of the volcano as evidence of active rifting followed by a phase of volcano growth and magma resurfacing when concentric grabens formed due to the volcano dynamics.

2.0 Geologic setting

2.1 Tharsis

Tharsis is the largest volcanic province of Mars and among the largest of the Solar System (Byrne, 2020). It spans an area of over 20 million km2, corresponding to ~25% of the whole Martian surface, and it comprises twelve large volcanoes from tens to hundreds of kilometres wide and up to 22 km high (e.g. Carr, 1973, Carr, 1974; Plescia, 2004; Werner, 2009; Yin, 2012). In particular, some of the shield

volcanoes developed on the utmost risen part of the Tharsis bulge, creating an elevated region of 7–11 km above the Martian datum (Yin, 2012). Within the Tharsis province are located the Tharsis Montes: three large volcanoes aligned NE-SW (Figure 1) that are from north to south and from the oldest to the youngest (Werner, 2009): Ascraeus Mons (18 km high and 300 km wide), Pavonis Mons (14 km high and 366 km wide) and Arsia Mons (19 km high and 470 km wide) -elevations and diameters from MOLA data (Plescia, 2004; Werner, 2009).

The three volcanic edifices of the Tharsis Montes are all elongated in the NE-SW direction, while Olympus Mons, the largest volcano in the Solar System is also close-by, just west of the Tharsis Montes (Figure 1). Alba Patera is instead located in the northernmost portion of the Tharsis province and it is a ~ 1000 km wide volcano with a relatively low altitude (~6 km). Other smaller volcanoes in the vicinity of Tharsis Montes are Uranius and Ceraunius Tholuses (e.g., Plescia, 2000), monogenic vents and other minor scoria/cinder cones such as the Ulysses Colles.

According to numerical modelling, the regional-scale large grabens radially extending from the Tharsis province and reaching a distance of ~4000 km are related to magma upwelling due to the presence of a mantle plume (Wilson and Head, 2002) or the combined action of topographic gradients and magmatic load (Bouley et al., 2016). Schultz et al. (2004) used MOLA topographic data to argue that at least some of these grabens are likely related to dyke intrusions and that generally large regional structures cannot be explained only by bulging without the presence of magma (Wilson and Head, 2002; Buchan and Ernst, 2019). Indeed, magmatic activity in the vicinity of these structures is widespread and lava flows channels along with grabens have been observed (Zimbelman and Edgett, 1991; Pozzobon et al., 2015). Moreover, large-scale grabens interpreted as evidence of dykes in the subsurface have been reported elsewhere in the Solar System such as on Venus (McKenzie et al., 1992; Grosfils and Head, 1994; Buchan and Ernst, 2019).

Based on crater counts analysis, the Tharsis Montes are believed to have formed during the Late-Hesperian through the Late Amazonian period (Scott and Tanaka, 1986). The main volcano formation ended about 3.55 Ga ago (Arsia Mons: 3.54 Ga; Pavonis Mons: 3.56 Ga; Ascraeus Mons: 3.6 Ga) and was followed by episodes of impact cratering (Werner, 2009). However, in the Tharsis volcanic province, only the last period of recent effusive eruption is constrained by surface ages derived from crater counts, showing prolonged but sporadic magmatic activities which continued until 200–100 Ma (Werner, 2009; Pozzobon et al., 2015).

Zhong (2008) hypothesizes that a slowly migrating hotspot and an associated plume of huge dimensions continuously fed the Tharsis volcanoes. The plume hypothesis is also supported by a geochemical study (Meyzen et al., 2014) based on analogies between hotspot volcanism on slow-moving plates and the Tharsis plume model.

Furthermore, the Tharsis province geologic history consists of six different phases of evolution generating intricate fault patterns, ranging from compressional to extensional, with radial and concentric orientation in the centre of the bulge (Bouley et al., 2016). Faulting occurred from early Noachian to late Amazonian with a peak of activity in the early Hesperian (Tanaka et al., 2014a, Tanaka et al., 2014b).

Reese et al. (2004) show that an impact-induced thermochemical plume, given a sufficiently large impactor, could have sustained volcanism for billions of years producing melt volumes and emplacement rates in broad agreement to those estimated for Tharsis. Alternatively, Yin (2012) suggests that a tectonic episode of slab rollback occurred, explaining the presence of the huge volcanic province as well as the alignment and spacing of the major Tharsis Montes volcanoes. According to this model, the rollback in the NW direction happened initially quite rapidly due to the voluminous amounts of melts and mantle upwelling, then a period of stationary subduction and reprise of the slab rollback occurred because of the snap of the slab due to thermal weakening close to the mantle-core boundary (Yin, 2012). These events would have first formed the Thaumasia region and Syria Planum volcanic zone, then the Tharsis alignment, and as a third phase the creation of the regional NE-SW graben zone of the Tharsis alignment and the Olympus Mons creation. The effect of having such large volcanic edifices on an isostatically compensated rise (Zuber, 2000) and a thickened lithosphere caused lithospheric flexure in the region of the Tharsis Montes inducing the development of "sagging" structures on the volcanoes as referred to by Byrne et al., 2009, Byrne et al., 2012, Byrne et al., 2013. Sagging structures consist of large imbricate "fish scale" patterns of lobate terraces and have been identified both on Mars as well as on Earth at Mauna Loa, Etna and Tendurek Dagi where similar lithospheric flexure occurs. Another consequence of the lithospheric flexure is the formation of a "dipole stress state" acting on a volcano (Watts, 2001; McGovern, 2007; Galgana et al., 2011; Byrne et al., 2012; McGovern et al., 2015) whereby compression of the volcano summit is coupled to extension at its base. The dipole stress state was also modelled with FEM showing that compressional structures at the volcano summit may prevent or limit caldera collapse (McGovern, 2007; McGovern and Morgan, 2009). Extensional structures at the base of the volcanoes appear to be often exploited by magma, as testified by the presence of elongated monogenetic vents with the direction of elongation parallel to the direction of the dyke intrusions (Byrne et al., 2012; Pozzobon et al., 2015). The formation of the three Tharsis Montes may have started with the growth of the main shield, followed by caldera collapse and formation of flank imbricate "fish scale" pattern terraces related to lithospheric flexure, which in turn caused extension at the base of the volcanoes where the most recent magmatic activity occurred (Byrne et al., 2012).

2.2 Pavonis Mons

Pavonis Mons, located at 1 N, 246E, is the central of the three Tharsis Montes volcanoes with an elevation above datum of ~14 km (Plescia, 2004). In plan view, it is slightly elliptical with the major axis ~ 350 km long oriented NW-SE and the minor axis ~ 300 km long oriented NE-SW.

The volcano summit consists of two nested calderas (Figure 2). The largest caldera is approximately 80 km in diameter while the smallest one is located on the south-western margin and it is ~35 km across (Robbins et al., 2011). The smallest caldera is steep-sided and flat-floored, while the largest caldera is bounded by a circular ridge with at least three NNE-SSW-trending wrinkle ridges (Scott et al., 1998). Faulting affects the rim of the large caldera and the wrinkle ridges are visible on the caldera floor. The large caldera was also filled by a lava lake whose age was calculated to be 130 ± 20 Ma (Robbins et al., 2011) in good agreement with previous measurements by Werner (2009) that tie the caldera infilling age at ~80 Ma. At the north-eastern side of the volcano two large lava aprons flowed in the NE-SW direction with very gentle slopes of ~1° following the Tharsis Montes alignment (At5 unit in Figure 2). Here, Pavonis is also cut by ~1.4 km deep elongated and steep-sided depression named Pavonis Chasma (Figure 2). The Pavonis Fossae is also present in the north-eastern sector: this is an ~30 km wide set of elongated depressions, ~1 km deep and up to 150 km long trending NW-SE almost perpendicular to the Tharsis Montes alignment (Scott et al., 1998). On the south-eastern flank of Pavonis (Figure 2), effusive structures often originate from large depressions, up to ~1.5 km in diameter, and create downstream wide, sinuous rilles (Scott et al., 1998). Some sinuous rilles originate from concentric grabens and therefore have been interpreted as dyke intrusions (e.g. Mège and Masson, 1996; Montesi, 2001; Wyrick and Smart, 2009).

Monogenetic cones largely cover Pavonis Mons, in particular on its south-western apron (Bleacher et al., 2009). On the flanks of the volcano, a subtle imbricate “fish scale” pattern, coherent with that described by Byrne et al., 2009, Byrne et al., 2012, Byrne et al., 2013, is visible on MOLA MEGDR topographic data as well as on THEMIS (Thermal Emission Imaging System) daytime IR global mosaic (100 m/pixel resolution) (Christensen et al., 2002; Edwards et al., 2011).

3.0 Data set and methods

In this work we mapped all the structural features of Pavonis Mons related to tectonics and volcano dynamics, we then analysed the fractures length distribution and the spatial distribution of structures, and we attempted to explain the topography with models of dyke injections and fault slips.

3.1 Mosaicking

The structural mapping has been carried out using both optical images and Digital terrain Models (DTMs). More specifically the image basemap was a mosaic of 76 overlapping images provided by the Mars Reconnaissance Orbiter CTX (Context Camera) (Malin et al., 2007). With its ~6 m/pixel of ground resolution and a swath width of ~30 km and a length variable between 50 and 300 km, this instrument provides data that are the best compromise between pixel resolution and spatial coverage since, up to date, it has covered more of 80% of the Martian surface. The images were processed using the USGS Integrated Software for Imagers and Spectrometers (ISIS 3) from the raw image files (Torson and Becker, 1997). We applied radiometric calibration, destriping/despiking to compensate both detector errors and vignetting effect. Images have been projected by attaching the satellite pointing for positioning the image at the right coordinates, via SPICE-kernels. In a second step, the images were mosaicked with the aid of an automatically generated grid of control points. To blend the images together seamlessly, we used the seamlines generated by ArcGIS mosaicking routine. This process employs the radiometry computational method that uses pixel values and pixel patterns in the overlapping portion of the images and stitches them together minimizing misalignments between the same features. The seamlines vector file was then used to stitch image portions as a jigsaw with an additional 10 pixels of blending on both sides of the seamline. Finally, the blended mosaic was output at 32-bit dynamic range to be able to stretch the images and to discern the structures.

3.2 MOLA DTMs

Most of the topographic data used in our work rely on the MOLA MEGDR gridded data (Mars Orbiter Laser Altimeter on board Mars Global Surveyor) (Smith et al., 2001), that present a grid size of ~463 m/pixel and a vertical resolution of 1 m. Given the large size of Pavonis Mons (~300 km in diameter), this was suitable for global-scale analyses given such high vertical resolution. However, for more detailed work on volcano-tectonic structures, we had to rely on a higher resolution dataset also in a grid format.

The profile curvature (*prof-c*) is the second derivative of the DTM and it is used to detect the rate of change of slopes along the direction of maximum steepness and, ultimately, to detect convexities and concavities (Wilson et al., 2007).

We calculated the *prof-c* with a kernel size of 15 pixels onto MOLA MEGDR (Mission Experiment Gridded Data Records) data on the whole volcanic edifice to detect large-scale curvature variations within the whole edifice with the *r.param.scale* GRASS module as shown in Fig. 3a, b (Wilson et al., 2007; Pozzobon et al., 2019). The large kernel size was chosen to compensate the effect that could be attributed to the presence of the imbricate “fish scale” pattern of lobate terraces

showed in Byrne et al., 2012, Byrne et al., 2013. After that, four sections passing for the centre of the volcanic caldera were analysed for profile curvature vs topography in order to explore changes in altitude (relative to the Mars datum) of the topographic setting (Figure 3a).

3.3 CTX DTMs

Detailed analyses of the volcano-tectonic structures and their relation to magma dynamics were carried out on specific areas where a higher resolution was possible. We selected CTX overlapping images on an area that host a wide range of structures, encompassing large deep arcuate grabens, small shallow grabens, pit chains and fissural vents.

The best overlapping CTX pairs (Table 1) were selected to obtain the best possible DTM, since CTX is not designed for stereo and therefore the DTM reconstruction is only possible when certain illumination conditions and stereo angles are met. Variations of these parameters control the quality of the DTM in terms of surface completeness and data noise.

The CTX images stereo-correlation was performed with ASP (Ames Stereo Pipeline) (Moratto et al., 2010). The stereo pair images were at first bundle adjusted to validate the DTM and subsequently generated to make the dataset usable for quantitative analyses.

MOLA PEDR (Precision Experiment Data Records) data corresponding to single laser shots before data gridding, thus presenting a higher vertical precision and no interpolated data, were used to align the point cloud obtained by stereo-matching using an ICP (Iterative Closest Point) algorithm. Then, the point cloud was gridded onto 18 m cells, following what is reported in Moratto et al. (2010) to gather the smoothest possible data at the highest possible resolution and, contextually, an orthoimage at 6 m/pixel was generated by using the left image of the stereo pair.

3.4 Mapping

Structures such as depressions, ridges, fractures and faults have been mapped as lines (Figure 4); besides, the median line of depressions, pit chains and grabens have also been recorded. Lava rilles and fissures were also mapped with particular attention paid to those that were emplaced in continuity with large grabens/pit chains (Figure 5 and Figure 6). Indeed, there are few examples of lava rilles emerging from deep grabens. Topographic highs, as ridges associated with the emersion of thrust's ramp (Figure 7), were also mapped at the summit of Pavonis together with the caldera structures. Barycentres of the structures were also calculated for spatial analyses.

3.5 Fault length size distribution

Experimental studies on normal fault populations suggest the presence of a lower (Lco) and an upper cutoff (Uco) in the power-law function describing the size-distribution of the geometric properties of fractures (e.g. Ackermann et al., 2001). Moreover, two or more power laws of length distributions can be observed in normal fault populations (e.g. Gudmundsson and Mohajeri, 2013).

Fault length distribution is often used to define the evolution of fault systems (e.g. Soliva and Schultz, 2008; Schultz et al., 2010; Mohajeri and Gudmundsson, 2012; Gudmundsson et al., 2013) and, in particular, two main length distributions are used to describe fault populations:

$$N (> L) = cL^{-a} \quad (1a)$$

$$N (> L) = \beta e^{-\lambda L} \quad (1b)$$

Where: N (> L) is the number of faults with length greater than L, c is the scaling factors and a the exponent for the power-law distribution (equation 1a), β and λ are the parameters of the exponential distribution (equation 1b). The following points should be accounted for when determining the parameters: (i) the error associated with the resolution limit of the measurements (truncation), and (ii) the error resulting from values of the measured features extending beyond the sampling window (censoring). Truncation leads to the underestimation of the contributions of measurements (e.g., length) below the resolution of the acquisition method (for example, fractures with a length lower than 20 m). The effect of censoring is the underestimation of measurements extending beyond the sampling window (e.g. a length greater than the area of the observation window). Comparison of the theoretical maximum values of the distribution with the maximum sampled value (|ΔLmax|) can thus indicate the influence of censoring and truncation; the higher the difference between these values, the higher is the influence of under-sampling. The theoretical maximum thickness could be derived by imposing N(Lmax) = 1 and solving for L (e.g., Mazzarini et al., 2011).

The vertical dimension of a fault (height) is nearly proportional to its length and is controlled by the mechanical layering of the crust as long as a sufficiently large contrast in material properties exists between the layers (Cowie and Scholz, 1992; Scholz et al., 1993; Cartwright et al., 1995; 1996; Benedicto et al., 2003; Soliva and Schultz, 2008; Gudmundsson et al., 2010). Two end-members for fault length distribution can be identified (Soliva and Schultz, 2008; Schultz et al., 2010): (i) localized fault systems, with few large faults cutting across the whole crust down to the main mechanical discontinuity, displaying a power-law distribution, and (ii) distributed fault systems, with strain regularly distributed along evenly spaced faults

and confined within specific mechanical layers in the crust, displaying an exponential distribution.

3.6 Fracture and vent self-similar clustering

In active volcanoes, the depth of the magma chamber from which dykes propagate toward the surface is a very important information to understand volcano dynamics (Gudmundsson et al., 2013). If the geometry of dykes is well constrained by field and geophysical data, their aspect ratio can be used to derive the driving fluid pressure and the depth of the magma source (Becerril et al., 2013). However, dykes shall not interact with other fractures and pure opening kinematics must be assumed (Gudmundsson, 1999, Gudmundsson, 2000). Such an approach is quite difficult when analysing a population of features with poorly known geometries, such as our studied cases, thus stochastic fractal analysis methods were used.

Fractal analysis is a methodology that uses observations of fractures or vents at the surface to infer the depth extent of fractures, assuming that migration of fluids such as magma occurs at depth (Mazzarini and Isola, 2010; De Toffoli et al., 2018).

Fractures' length and their spatial distribution control the overall permeability of fracture networks (Darcel et al., 2003). The percolation theory quantifies a critical fracture density threshold that defines the limit above which the fracture network is connected (Mazzarini and Isola, 2010). When the fracture network is percolating its spatial distribution is fractal and its self-similarity is defined in a specific lengths range bounded by a lower and an upper cutoff (e.g. Mandelbrot, 1982). This analysis is done to evaluate the scaling properties of the systems and, in particular, to derive the upper cutoff assumed to represent the distance between the surface and the fluid source at depth (e.g. Mazzarini and Isola, 2010). We performed self-similar clustering (i.e. how the features fill the space) of the datasets of interest by applying the following scaling equation:

$$C(L)=aL^{D}$$

where C(l) is the correlation sum, defined as C(L) = 2 N(L)/(N(N-1)) where N(L) are the pairs of points whose distance is less than L, and D is the fractal exponent. This method has been implemented on fracture barycentre (Bour et al., 2002). Notably, the derivation of the two-point correlation dimension is statistically dominated by the numerous small fractures, for which the error in the determination of the precise spatial location is relatively insignificant. The D exponent is defined as the slope of the log(C(L)) vs. log(L) curve (eq. (2)); high D values imply increasingly homogeneous distribution of fractures, low values imply increasingly clustered distribution of fractures (Bonnet et al., 2001; Darcel et al., 2003; Mazzarini and Isola, 2010). The size range, bound within the lower and upper cutoffs, is detectable as a

linear fit (a plateau) in a local slope $\Delta\log(C(L)/\Delta\log(L))$ vs. $\log(L)$ diagram (Walsh and Watterson, 1993). The Uco (upper cutoff; i.e. the highest plateau breaking point) is defined by the maximum value of the size range with the highest R2 (Mazzarini, 2004). To produce statistically significant estimates at least 50 samples are commonly required (Clauset et al., 2009). We performed analyses on clusters exceeding the minimum number of 50 units, thus keeping the error on the scaling parameter smaller than 1%. Since the upper cutoff (Uco) scales as the maximum thickness of the medium between the surface and the reservoir at depth, this is the specific parameter to investigate to understand possible fracturing mechanisms, e.g. depth of the plumbing system, shallow fracturing, or overpressure fracturing (Mazzarini and Armienti, 2001; Mazzarini and Isola, 2010; Pozzobon et al., 2019).

4. Brittle structures

Faults, grabens and pit chains characterize Pavonis Mons volcano as well as its surroundings (Scott et al., 1998). Extensional features appear to be concentric to the shape of Pavonis and concentrated at the slope change at the base of the volcano, often exhibiting very well-developed concentric sets of km-wide grabens and normal faults that can be up to 200 km-long. On the north-western and south-eastern sides of Pavonis, there are sets of grabens up to 5 km wide, more than 100 km long and a few hundreds of meters deep. The widest structures are located in the north-western flank and are almost equally spaced sets of horsts and grabens that tend to increase in number moving northward, up to the point that structures are no longer distinguishable as horst-graben alternations. Instead the structures appear as sets of tens of evenly-spaced NW-verging normal faults, and in a few cases relay ramps that correspond to overstepping fault segments (Figure 4b).

The south-eastern structures follow the same concentric pattern, but the grabens are much less wide (~1 km or less) and steeper. They appear organized in parallel sets often characterized by the presence of aligned collapse pits that in several cases coalesce and merge into a larger/longer structure (Figure. 4d, 5 and 6). In this sector, as in the south-western flank, the deepest grabens present lava rilles and lava flows originating from them, and in few cases (Figs. 4c, 5 and 6) they can be found in correspondence (or in continuation) of fissure vents.

5. Volcano summit zone

Pavonis Mons and its surroundings are characterized by faulting, grabens, pit chains, lava tube, lava flows as well as fan-shaped deposits at the toe of the edifice, and small volcanic fields (Shean et al., 2005; Bleacher et al., 2009). Also, the summit of

Pavonis Mons shows a very complex structural setting consisting of two-nested calderas (Scott et al., 1998), with the smaller younger caldera that grew in the south-western part of the larger and older caldera (late Amazonian age; Robbins et al., 2011) (Figure 7).

The rims of the older, larger caldera are strongly asymmetric; its north-eastern sector is uplifted showing topography very similar to wrinkle ridge, whereas the rim in its north-western sector has a smooth topography and connects gently to the caldera floor (Figures 7a, c). Normal faults affect the western and southern sectors of the rim (Figure 7a). Moving toward southeast and southwest, i.e. along the southern sector of the caldera rim, its topographic expression is overprinted by the growth and formation of the younger caldera (Figures 7a, c).

Normal faults with a principal NE-SW trend (Figure 8a) occur at the older caldera rim and the northwestern rim of the younger caldera (Fig. 7) but compressional features, like wrinkle ridges (Schultz, 2000; Mueller and Golombek, 2004), are also present in the volcano summit and crosscut by such faults; they display a radial pattern (Figure 8b) suggesting that they are not coeval.

A large curved fault (about 60 km long) cuts the floor of the older caldera with a direction varying from SW to ENE (Figures 7a, c). The portion of the fault striking ENE-WSW displaces through an apparent dextral offset, a wrinkle ridge (Figures 7b, c), while its NE-SW striking portion cuts the rim of the younger caldera with an apparent normal faulting displacement (Figure 7c). Such geometries suggest that, after the formation of the two calderas and the N-S wrinkle ridges, a normal fault formed close to the rim of the small young caldera and became oblique as the strike of the faults rotates.

Shallow grabens are often colinear with deeper grabens and separated by pit chains along the same fault line. Although such shallow and deep grabens have been mapped based on their morphological convergence, they may represent different stages of an evolutionary process (Figure 6). Concentric grabens are typically topographically shallow (Figure 4a), but if the faults become dilatant, collapse pits can form along them (Figure 4e). If dilatant conditions persist, collapse pits will grow to form along axis pit chains, and eventually merge into larger depressions that, visually, appears as a topographically deeper graben. Dilatant faults can be either formed by dyke injections or they can be exploited by dykes after their formation, eventually transforming the faults into along axis emission centers of sinuous rilles (Figure 6).

6. Spatial analysis

The spatial analysis of grabens and pit-chains in Pavonis Mons has been performed in terms of length size distribution, self-similar clustering and azimuth distribution. Two main distributions can be used when analysing fault population statistics: size distribution and spatial distribution. The former focuses on the geometric properties of features such as fault length or displacement, while the latter analyses the properties of the whole population by relating each fault to the others, such as fault density and clustering.

As for Ascraeus Mons (Pozzobon et al., 2015), we used the traces of grabens and pit chains (Figure 3a) as a proxy for dykes and we applied the self-similar clustering analysis. The analysed data sets consist of a total of 493 mapped grabens and pit chains, of which the grabens are 390 and the pit chains are 103. Apart from the clear morphologic differences between grabens and pit chains, we decided to analyse grabens independently for their length size distribution and self-similar clustering, because they may result from extensional tectonics (Figure 4a), magmatic activity or both. The latter case occurs when magma migrates along a pre-existing structure after carving it deeply by lava thermal erosion (Figures 4b, 5a, b and 6), or when faults, reaching up to tens of kilometres deep (Ferrill et al., 2004), form above a dyke and create at the surface pit chains with no magma erupted (Wyrick and Smart, 2009).

6.1 Length size distribution

The whole data set (Table 2) shows an exponential length distribution in the 0.7–132 km range with a maximum observed length of ~133 km and a maximum theoretical length of 154 km. Grabens show a well-defined exponential length distribution in the size range of 2.3–132 km with a maximum observed length of 132.6 km and a maximum theoretical length of 148.8 km (Table 2).

Pit chains have a power-law length distribution in the size range of 6.5–55 km with the fractal exponent of 1.6 and the maximum observed length of 105.7 km while the maximum theoretical length is 106.7 km (Table 2).

6.2 Self-similar clustering

The self-similar clustering of all mapped structures shows fractal exponent of 1.6736 with a size range of 0.5–95 km (Figure 9a). The self-similar clustering of grabens (Figure 9b) is characterized by the high fractal exponent (1.98) in the range 1.8–20 km (Table 3). Pit chains (Figure 9c) show self-similar clustering in the 12–100 km size range with a low value of the fractal exponent (1.33; Table 3).

6.3 Azimuth distribution

Grabens and pit chains in Pavonis Mons show azimuth distributions characterized by few, well-defined peaks. Grabens have main peaks trending N50°E and N15°E, minor peaks trend N-S and N30°W, while very few grabens have trend in the ENE-ESE sector (Figure 10a, left panel). Pit chains show two well-defined peaks trending N-S and N50°E and a minor peak trending N50°W (Figure 10b, left panel).

The grabens and pit chains in Pavonis Mons show different azimuth distribution from the lower elevations at the foot of the volcano (4000 m) to its summit zone (14,000 m). Most of the structures located at elevations less than 9 km (right panels in Figure 10a) display an asymmetry in the elevation distribution with a possible trade-off elevation at 9 km (Figure 10b). To understand if the 9 km threshold in the elevation distribution (Figure 10, right panels) has a geological meaning we performed the analysis of elevation versus curvature (i.e. convexity and concavity of the volcano flanks) along 2 pairs of orthogonal topographic profiles (Figure 3a), crossing the volcano summit (Figures 3c and d). The main changes in curvature along the four profiles occur at the 9 km elevation corresponding to the elevation of the caldera complex floor (Figures 3c and d). The azimuth distributions of grabens and pit chains have thus been analysed using an elevation threshold of 9 km (Figures 3e and f). This value was chosen because the grabens or pit chains below the elevation of 9 km (left panels in Figures 3e and f) show N-S and NE-SW trends with less dispersion and noise than that resulting from the analysis of the whole dataset (Figure 10). The orientation of the structures above 9 km elevation show a clear radial pattern (Figures 3e and f, right panels).

7. Topographic modelling

We analyzed the topography to determine what type of magmatic and tectonic sources may have played a role in constructing the current topography. A high-resolution DEM was extracted on a sector of Pavonis and we selected for the modelling an area with a graben over 10 km long and 500 m deep on the flank of Pavonis Mons (Figure 11). To match the observed topography, we tested models of dyke intrusion, faulting and dyke-induced faulting above a dyke (Okada, 1985), assuming the conventional elastic half-space model with a Poisson's ratio of 0.25. For our modelling we used only the surface vertical displacements caused by the different source models, therefore our results of dyke width and fault slip should be considered upper bounds. The reason for not including horizontal displacements in our models is because we want to compare the dyke and faulting models. For a dyke intrusion, the graben width can be modelled by the dyke extension, while this is not possible for the extensional tectonic case where the width of the graben is just the

result of where the border faults initially develop. Therefore, to make the different models comparable we only used the vertical component of the displacement in our models. We found the best-fit model parameters using a nonlinear inversion, employing a Monte Carlo simulated annealing algorithm that has been widely used to model volcanic and rifting deformations (e.g., Cervelli et al., 2001; Pagli et al., 2015; Barnie et al., 2015). Before performing the inversion, the topography was cleaned from the slope by subtracting a linear tilt (Figures 12a-c) and the data were then quadtree partitioned (Figure 12d) to reduce the data size.

Initially, we tested a vertical dyke model and found a best-fit solution for an 11 km long, ~NNE-WSW trending dike extending from 1.5 km below the surface to 100 km depth with a uniform opening of 2800 m (Figures 13a-c). The model can explain the main topographic low but there are relatively high residuals on its flanks where model predictions are for significant uplift. We then tested a model with two faults dipping towards the central axis of the graben and we found that two sub-vertical normal faults 15 km long and 14 km deep with 400 m of dip-slip can better explain the topographic low. Conversely, the faults model does not explain any of the flank uplift where the elevated topography remains unpredicted by this model (Figures 13d-f). We finally tested a model of a dyke-induced graben with a vertical dyke and two dyke-dipping normal faults on top of it. The dyke is 15 km long, it is located under the centre of the main topographic low and extending from 1.4 km below the surface to 83 km depth with a uniform opening of 500 m. The two normal faults on either side of the dyke are 10 and 15 km long respectively, and both are 10 km deep and have about 390 m of dip-slip. This model explains the central subsidence and the elevated topography on the flank of the graben better than the other models, thus we conclude that dykes likely occured under the graben but were thin and did not cause much uplift of the flanks while the normal faults mainly contributed to the surface topography generating steep and deep grabens.

8. Discussion

The azimuth distribution of grabens (Figure 3) shows different patterns depending on the elevation. Grabens developed above the 9 km of elevation, i.e. at an elevation greater than that of the caldera floor, show a concentric pattern (whose azimuths are homogeneously distributed) consistent with inflation and/or deflation dynamics of the volcano. On the other hand, grabens at an elevation lower than 9 km have a distribution with a well-defined NE-SW trend, parallel to the alignment of the Tharsis Montes. These different patterns of graben azimuthal distribution are interpreted as the result of initial active rifting with the formation of linear grabens at the base of the volcano, followed by a phase of volcano growth and magma resurfacing when concentric grabens formed due to the prevailing volcano dynamics. Pavonis Mons

thus records both regional and local (volcano dynamics) deformations, which is particularly active in its summit, where faults affect the caldera rims producing a marked asymmetry in the outer caldera rim and formation of wrinkle ridges. The pattern of wrinkle ridges along with the development of the large fault across the outer caldera may result from the sum of different phases of shortening, where the later compressive deformation occurred in the south-eastern sector of the old caldera, probably linked to the strike-slip kinematic of the WSW-ESE strike-slip fault offsetting the N-S striking wrinkle ridges. Large faults dissecting the volcano edifice with changing along strike kinematics may accommodate volcano dynamic/instabilities, as observed at the Pernicana fault in Etna volcano, Italy (Currenti et al., 2010).

Crustal thickness in the Tharsis Montes area is approximately 75 km (Montesi and Zuber, 2003; Ruiz et al., 2011), assuming only conductive heat transfer and the heat flow for the area of Pavonis Mons in late Amazonian varying from 25 to 30 mWm−2 and an average thermal conductivity for the Martian basaltic crust of 2Wm−1 K−1 (values from Ruiz et al., 2011) a minimum geothermal gradient for the Pavonis Mons area is in the 15–13 C°km−1 range. Because Pavonis Mons is in a volcanic area convective and advective processes are likely to have occurred producing higher geothermal gradient with values consistent with temperatures of 400–500 C° or higher than 500 °C at 20 km depth, very close to or at the brittle-ductile transition zone for plagioclase (Voll, 1976) or basalt (Violay et al., 2012), respectively.

The difference between the theoretical and observed maximum length (|ΔLmax|; Table 2) of the negative exponential length size distribution of the brittle structures (grabens plus pit chains) suggests that there is a problem of truncation and that, probably, they cannot be analysed as a unique data set. Notably, the very scattered spectrum for length less than ~20 km for the spatial clustering of the whole data set (Figure 9a) indicates that the two structures cannot be easily related to the evolution of a common fracture network. Also, grabens alone have a negative exponential length size distribution (Table 2) with high |ΔLmax| value suggesting that they suffer from truncation and that probably their formation and evolution could be due to different processes may be acting at different times (tectonics and/or magmatism for example). On the other and, the pit chains size length distribution has a very low |ΔLmax| indicating that the analysed sample represents well the population of pit chains. The length size distribution of grabens may indicate that they are confined within a mechanical layer of the crust, likely very upper brittle crust (Schultz et al., 2010), while pit chains show a clear power-law size length distribution (Table 2) indicating that their associated structures cut across the whole crust. The analysis of self-similar clustering (Table 3) suggests that the associated fault network may reach a depth of 20 km for grabens while for pit chains a depth of 100 km is in good agreement with results from the size distribution of the structures. The grabens are

thus structures that formed in the very upper brittle crust in the Tharsis Montes area, while the structures associated with the pit chains formation cut across the whole crust.

The analysis of the self-similar clustering (Table 3) shows that grabens have higher fractal exponent (D = 1.97) than pit chains (D = 1.33), implying that pit chains are much more clustered than grabens. We interpret the pit chains as an expression of the main feeder structures withdrawing magma from deep subcrustal reservoirs (Pozzobon et al., 2015). Grabens could have acted as pathways for dyke intrusions sourced from shallower reservoirs and affecting the volcanic edifice. We suggest that the grabens possibly captured dykes rising from deep reservoirs. The capture of dikes en-route to the surface by faults is a well-known mechanism at central volcanoes and volcanic fields (Gafney et al., 2007; Maccaferri et al., 2015). In support of this interpretation we observe the magma flowing out of the narrower grabens (Figure 4c). All these observations are consistent with models of dyke intrusions with dyke-induced faulting above the dyke. We notice that our dyke models predict more uplift on the flanks of the intrusions than observed, suggesting that faulting occurred above thin dykes.

9. Conclusions

In this study, we analyzed grabens and pit chains associated with Pavonis Mons in the Tharsis volcanic province on Mars. From the analysis of their topographic distribution, azimuth, size distribution and clustering we were able to discern whether they are the result of tectonics related to Tharsis province activity or internal volcano dynamics. The analyses show that faults related to large grabens are confined in a mechanical layering in the upper layers of the brittle crust, whereas deeper structures such as pit chains are most likely associated to magma injection/dykes and therefore, connected to the subcrustal magma source at a depth of ~80–100 km. Therefore, based on our results, we infer that Pavonis Mons recorded active rifting at the initial stages of development with the formation of the large graben and faults at its base, but then the growth of a central volcano and the dynamics of the magma chamber dominated the structural features.

Acknowledgements

C.P. acknowledges support by the University of Pisa grant PRA_2018_19.

Data availability

All the planetary data used in this paper are freely available at NASA PDS Geosciences Node at https://pds.nasa.gov and high-level processed products (MOLA MEGDR) are available at the USGS Astrogeology Science Center https://www.usgs.gov/centers/astrogeology-science-center.

Raw CTX image processing, mosaicking and custom DTMs were generated through USGS Astrogeology ISIS3 software (https://isis.astrogeology.usgs.gov) and Ames Stereo Pipeline plugin https://ti.arc.nasa.gov/tech/asr/groups/intelligent-robotics/ngt/stereo

Figure and Table captions

Figure 1. MOLA DEM (463 m/pixel) topography of the Tharsis area draped on the shaded relief from the same dataset

Figure 2. Geologic map of Pavonis from Scott et al. (1998) draped on THEMIS daytime infrared image with highlighted the main geologic units. As: smooth material occupying low topographic areas; Ak: knobby, hilly, and hummocky terrains; Ake: elongated ridged material; Ac: fresh craters,with clear ejecta deposits and raised rim; At4: highly faulted central shield of Pavonis Mons, presenting grabens, faults and fissures. It corresponds to the Ave unit of Amazonian age shields in Skinner et al., (2016); At5: prominent lava flow lobes and rough surface, it underlies and is in contact with Ak unit. This unit corresponds to the Amazonian-Hesperian volcanic unit described in the map by Skinner et al., (2016); At6: fresh-appearing lava flows filling the central caldera and overlying partially the At4 unit on the southern side of the volcano; AHt3: deeply eroded lava flows.

Figure 3. Topographic map and curvature profiles of Pavonis Mons. The profiles are 500 km long and are taken across the center of the summit caldera, each profile is separated by 30° of azimuth.
a) The MOLA MEGDR at 463 m/pixel shaded relief with overlaid the profile curvature calculated on a 15x15 kernel size. In blue are the concavities and in red the convexities. **b)** 3D view of Pavonis with 3x vertical exaggeration. **c)** N-S and E-W topographic profiles shown in a). For N-S profile: black line is the elevation and the open black circle is the curvature along the profile. For the E-W profile: red line is the elevation and the red cross is the curvature along the profile. **d)** ENE-WSW and SSE-NNW topographic profiles shown in a). For the ENE-WSW profile: black line is the elevation and the open black circle is the curvature along the profile. For the SSE-NNW profile: red line is the elevation and the red cross is the curvature along the profile. The dashed black line is the 9 km elevation, the base of the caldera floor. **e)** Rose diagram of the grabens with barycenter at elevation < 9 km (left-panel), and rose diagram of the grabens with barycentre at elevation > 9 km (right-panel). f) Rose

diagram of the pit chains with barycenter at elevation < 9 km (left-panel), and rose diagram of the pit chains with barycentre at elevation >9 km (right-panel).

Figure 4. Structures mapped on Pavonis Mons using a combination of MOLA topography, THEMIS IR mosaics and CTX image mosaic. **a)** complete structural mapping, overlaid on THEMIS global mosaic daytime infrared. Illumination direction is from the NW. **b)** set of parallel normal faults with NW vergence of the fault planes. Two large grabens are visible in the central/eastern part of the image with a relay ramp on the left side of the first large graben. Isolated normal faults are mapped as yellow lines and the graben central axes are mapped as green lines in a). **c)** set of both shallow large grabens and a deeper graben from which departs a sinuous rille carved by low-viscosity basaltic lava flow. We counted > 20 similar examples on the whole Pavonis edifice where pre-existing structures are preferential pathways for dyke injection and lava emission. These structures are marked with cyan lines in a), also relay ramps are also visible in the central part of the image. **d)** A large shallow graben on the westernmost part of the image and in the central part, a graben evolving into a pit chain, where the hybrid/dilatant behaviour of the fault causes the formation of collapse pits where loose material on the surface fall in. Eventually, these will coalesce forming deeper and narrower structures. Axes of pit chains are marked as red lines in a). **e)** A graben with collapse pits forming along one of its border faults, testifying a transition from normal fault to dilatant fault. A skylight in proximity of the other bordering fault is likely an incipient collapse that will evolve into a larger pit caused by dilatant fault and then filled with loose material. Beneath such collapses dykes can be stalling, unable to reach the surface as for shown in c).

Figure 5. Examples of concentric structures on the south-western flank of Pavonis Mons. It is visible how deep grabens can be exploited by lava, and if the magma supply is sufficiently high, grabens can become emission centers. **a)** Pit chains coalescing and ultimately merging into single deeper grabens. In the central part of the image a deep collapse, aligned with smaller structures acts as an emission center creating a NNE-SSW sinuous rille. **b)** Sub-parallel coalescent pit chains becoming emission centers if dykes reach the surface.

Figure 6. A set of concentric grabens in the north-eastern side of Pavonis. In the uppermost portion it can be seen how a topographically shallow graben, if stress conditions become dilatant, can lead to formation of collapse pits, aligned along the structure. Eventually, as pits continue to grow they would coalesce and merge and start appearing as a deeper graben. Opening of such structures is caused either by dyke injections or is later exploited by lava. The structures become a locus of magma output leading to sinuous rilles formation (right-hand side of the figure). The image and the context image of Pavonis are both oriented 90° clockwise for a better display.

Figure 7. Summit calderas of Pavonis Mons (CTX image mosaic). **a)** The red line marks the rim of the youngest and smallest caldera and A its centre. The orange line marks rim of the oldest and largest caldera and B its centre. Yellow lines are the main faults; blue lines are wrinkle ridges and white boxes mark the location of the areas shown in b-c). **b)** CTX image mosaic of a fault in the oldest caldera cutting across a wrinkle ridge with apparent dextral strike-slip motion (the slip is marked by yellow arrows and offset represented by A-A'). **c)** CTX image of the same fault as in b) but cutting across the rim of the youngest caldera with apparent normal offset.

Figure 8. **a)** Rose diagram of azimuth distribution of normal faults in the summit of Pavonis Mons. **b)** Rose diagram of azimuth distribution of wrinkle ridges in the summit of Pavonis Mons.

Figure 9. Self similar clustering (log plot of C(l) vs. l) **a)** of all the concentric structures mapped on the flanks of Pavonis Mons, **b)** of the grabens and, **c)** of the pit chains. Black crosses are the local slope representing the fractal exponent D (Table 3). The fractal exponent is computed in a size range defined by the plateau in the log(l) vs. local slope plot highlighted by the shaded area (i.e. where D is almost constant) and whose maximum and minimum values are identified by a lower cutoff (Lco) and an upper cutoff (Uco), (eq. 2, and Table 3).

Figure 10. Azimuth and elevation distributions of grabens and pit chains in Pavonis Mons. **a)** Left panel: azimuth distribution of grabens. Right panel: histogram of elevation of grabens, dashed black line is the Gaussian distribution fit, the solid vertical black line is the 9 km elevation. **b)** Left panel: azimuth distribution of pit chains. Right panel: histogram of elevation of pit chains, dashed black line is the Gaussian distribution fit, the solid vertical black line is the 9 km elevation.

Figure 11. **a)** THEMIS daytime infrared image draped onto MOLA DEM. The white box marks the position of the CTX DEM shown in **b)** MOLA DEM image of the graben selected for modelling. In the lower panel topographic profile of the CTX DEM (18 m/pixel) highlights the depth of the graben.

Figure 12. Slope correction. **a)** Original topography. **b)** The fitted slope on the area. **c)** The corrected topography obtained by subtracting the slope shown in b) from the original topography in a). **d)** Downsampled topography after quadtree partition.

Figure 13. Topographic models. **a-c)** Are the dyke model, **d-e)** are the two normal faults model, **g-l)** are the dyke-induced graben with a dyke intrusion and two normal faults. The colour bar in the upper right corner applies to all images.

Table 1. CTX stereo pair used to generate the DTM for the topographic modelling. The expected vertical precision and convergence angle are calculated with the tool provided in PILOT website by USGS (pilot.wr.usgs.gov).

Table 2. Statistics of the length size-distribution of grabens and pit chains.

Table 3. Statistics of the self-similar clustering of grabens and pit chains.

References

Ackermann, R.V., Schlinsche, R.W., Withack, M.O., 2001. The geometric and statistical evolution of normal fault systems: An experimental study of the effects of mechanical layer thickness on scaling laws. *Journal of Structural Geology*, 23, 1803-1819. https://doi.org/10.1016/S0191-8141(01)00028-1

Acocella, V., Neri, M., 2009. Dike propagation in volcanic edifices: Overview and possible developments. *Tectonophysics*, 471, 67-77. ttps://doi.org/10.1016/j.tecto.2008.10.002

Barnie, T.D., Oppenheimer, C., Pagli, C., 2015. Does the lava lake of Erta 'Ale volcano respond to regional magmatic and tectonic events? An investigation using Earth Observation data. *Geological Society Special Publication*, 420(1), 181-208. https://doi.org/10.1144/SP420.15

Becerril, L., Galindo, I., Gudmundsson, A., Morales, J.M., 2013. Depth of origin of magma in eruptions. *Sci. Rep*. 3, 1–6. https://doi.org/10.1038/srep02762

Benedicto, A., Schultz, R.A. and Soliva R., 2003. Layer thickness and shape of faults. *Geophysical Research Letters*, 30, 20, 2076, https://doi.org/10.1029/2003GL018237

Bistacchi, A., Tibaldi, A., Pasquarè, F. a., Rust, D., 2012. The association of cone–sheets and radial dykes: Data from the Isle of Skye (UK), numerical modelling, and implications for shallow magma chambers. *Earth Planet. Sci. Lett*. 339–340, 46–56. https://doi.org/10.1016/j.epsl.2012.05.020

Bleacher, J.E., Glaze, L.S., Greeley, R., Hauber, E., Baloga, S.M., Sakimoto, S.E.H., Wiliams, D.A., Glotch, .D., 2009. Spatial and alignment analyses for a field of small volcanic vents south of Pavonis Mons and implications for the Tharsis province, Mars. *Journal of Volcanology and Geothermal Research*, 185, 96–102. https://doi.org/10.1016/j.jvolgeores.2009.04.008

Bonnet, E., Bour, O., Odling, N.E., Davy, P., Main, I., Cowie, P., Berkowitz, B., 2001. Scaling of fracture systems in geological media. *Reviews of Geophysics*, 39 (2001), 347-383. https://doi.org/10.1029/1999RG000074

Bouley, S., Baratoux, D., Matsuyama, I., Forget, F., Séjourné, A., Turbet, M., Costard, F., 2016. Late Tharsis formation and implications for early Mars. *Nature* 531, 344–347. https://doi.org/10.1038/nature17171

Bour,O., P., Darcel, C., Odling, N., 2002. A statistical scaling model for fracture network geometry, with validation on a multiscale mapping of a joint network (Hornelen Basin, Norway). *Journal of Geophysical Research*, 107, 2113, https://doi.org/10.1029/2001JB000176

Buchan, K., L., Ernst, R., E., 2019. Dyke Swarms of the World: A Modern Perspective, Dyke Swarms of the World: A Modern Perspective, Springer Geology. Springer Singapore. https://doi.org/10.1007/978-981-13-1666-1

Byrne, P. K., van Wyk de Vries, B., Murray, J. B., Troll, V. R., 2009. The geometry of volcano flank terraces on Mars. *Earth and Planetary Science Letters* 281, 1–13, http://dx.doi.org/10.1016/j.epsl.2009.01.043

Byrne, P.K., van Wyk de Vries, B., Murray, J.B., Troll, V.R., 2012. A volcanotectonic survey of Ascraeus Mons, Mars. *J. Geophys. Res*. 117, E01004. https://doi.org/10.1029/2011JE003825

Byrne, P.K., Holohan, E.P., Kervyn, M., Van Wyk de Vries, B., Troll, V.R., Murray, J.B., 2013. A sagging-spreading continuum of large volcano structure. *Geology* 41, 339–342. https://doi.org/10.1130/G33990.1

Byrne, P.K., 2020. A comparison of inner Solar System volcanism. *Nat. Astron*. 4, 321–327. https://doi.org/10.1038/s41550-019-0944-3

Carr, M. H., 1973. Volcanism on Mars. *J. Geophys. Res*., 78, 4049–4062. https://doi.org/10.1029/JB078i020p04049

Carr, M.H., 1974. Tectonism and volcanism of the Tharsis region of Mars. *J. Geophys. Res*. 79, 3943–49. https://doi.org/10.1029/JB079i026p03943

Cartwright, J. A., B. Trudgill, and C. S. Mansfield 1995. Fault growth by segment linkage: An explanation for scatter in maximum displacement and trace length data from the Canyonlands Grabens of SE Utah. *J. Struct. Geol.*, 17, 1319–1326. https://doi.org/10.1016/0191-8141(95)00033-A

Cervelli, P., Murray, M.H., Segall, P., Aoki, Y., Kato, T., 2001. Estimating source parameters from deformation data, with an application to the March 1997 earthquake swarm off the Izu Peninsula, Japan. *J. Geophys. Res. Solid Earth* 106, 11217–11237. https://doi.org/10.1029/2000jb900399

Clauset, A., Shalizi, C.R., Newman, M.E.J., 2009. Power-law distributions in empirical data. *SIAM Review*, 51, 661–703. https://doi.org/10.1137/070710111

Cowie, P. A., and C. H. Scholz (1992), Physical explanation for the displacement-length relationship of fault using a post-yield fracture mechanics model. *J. Struct. Geol*., 14, 1133– 1148, https://doi.org/10.1016/0191-8141(92)90065-5

Currenti, G., Bonaccorso, A., Del Negro, C., Guglielmino, F., Scandura D., Boschi, E., 2010. FEM-based inversion for heterogeneous fault mechanisms: application at Etna volcano by DInSAR data. *Geophysical Journal International*, 183, 765-773. https://doi.org/10.1111/j.1365-246X.2010.04769.x

Darcel, C., Bour, O., Davy, P., de Dreuzy, J.R., 2003. Connectivity properties of two-dimensional fracture networks with stochastic fractal correlation. *Water Resources Research*, 39, 1272. https://doi.org/10.1029/2002WR001628

De Toffoli, B., Pozzobon, R., Mazzarini, F., Orgel, C., Massironi, M., Giacomini, L., Cremonese, G., 2018. Estimate of depths of source fluids related to mound fields on Mars. *Planetary and Space Science*, 164, 164–173. https://doi.org/10.1016/j.pss.2018.07.005

Edwards, C. S., K. J. Nowicki, P. R. Christensen, J. Hill, N. Gorelick, and K. Murray (2011), Mosaicking of global planetary image datasets: 1. Techniques and data processing for Thermal Emission Imaging System (THEMIS) multi-spectral data. *J. Geophys. Res.*, 116, E10008, doi:10.1029/2010JE003755. https://dx.doi.org/10.1029/2010JE003755

Ernst, R., Desnoyers, D., Head, J., Grosfils, E., 2003. Graben-fissure systems in Guinevere Planitia and Bata Regio (264–312E, 24–60N), Venus, and implications for regional stratigraphy and Mantle Plumes. *Icarus* 164, 282–316. https://doi.org/10.1016/S0019-1035(03)00126-X

Ferrill, D.A., Wyrick, D.Y., Morris, A.P., Sims, D.W., Franklin, N.M., 2004. Dilational fault slip and pit chain formation on Mars. GSA Today 14. https://doi.org/10.1130/1052-5173(2004)014%3C4:DFSAPC%3E2.0.CO;2

Galgana, G. A., McGovern, P.J.& Grosfils, E.B. 2011. Evolution of large Venusian volcanoes: insights from coupled models of lithospheric flexure and magma reservoir pressurization. *Journal of Geophysical Research*, 116, E03009, https://doi.org/10.1029/2010JE003654

Galgana, G.A, Grosfils, E.B., McGovern, P.J., 2013. Radial dike formation on Venus: Insights from models of uplift, flexure and magmatism. *Icarus*, 225, 538-547. https://doi.org/10.1016/j.icarus.2013.04.020

Grosfils, E.B., Head, J.W., 1994. The global distribution of giant radiating dike swarms on Venus: Implications for the global stress state. *Geophys. Res. Lett.* 21, 701–704. https://doi.org/10.1029/94GL00592

Grosfils, E.B., Mcgovern, P.J., Gregg, P.M., Galgana, G.A., Hurwitz, D.M., Long, S.M., Chestler, S.R., 2015. Elastic models of magma reservoir mechanics: A key tool for investigating planetary volcanism. *Geol. Soc. Spec. Publ.* 401, 239–267. https://doi.org/10.1144/SP401.2

Gudmundsson, A., 1999. Fluid pressure and stress drop in fault zones. *Geophys. Res. Lett.* 26, 115-118. https://doi.org/10.1029/1998GL900228

Gudmundsson, A., 2000. Fracture dimensions, displacement and fluid transport. *Journal of Structural Geology*, 22, 1221–1231. https://doi.org/10.1016/S0191-8141(00)00052-3

Gudmundsson, A., Loetveit, I.F., 2005. Dyke emplacement in a layered and faulted rift zone. *J. Volcanol. Geotherm. Res*. 144, 311–327. https://doi.org/10.1016/j.jvolgeores.2004.11.027

Gudmundsson, A., Friese, N., Galindo, I., Philipp, S.L., 2008. Dike-induced reverse faulting in a graben. *Geology* 36, 123–126. https://doi.org/10.1130/G24185A.1

Gudmundsson, A., and Mohajeri, N., 2013. Relations between the scaling exponents, entropies, and energies of fracture networks. *Bull.Géol. France*, 2013, 184(4), 373-382. https://doi.org/10.2113/gssgfbull.184.4-5.373

Gudmundsson, A., De Guidi, G., and Scudero, S., 2013. Length-displacement scaling and fault growth. Tectonophysics, 608, 1298-1309. https://doi.org/10.1016/j.tecto.2013.06.012

Gudmundsson, A., Simmenes, T.H., Larsen, B. and Philipp, S.L., 2010. Effects of internal structure and local stresses on fracture propagation, deflection and arrest in fault zones. *Journal of Structural Geology*, 32, 1643-1655. https://doi.org/10.1016/j.jsg.2009.08.013

Jónsson, S., Zebker, H., Segall, P., Amelung, F., 2002. Fault slip distribution of the 1999 Mw 7.1 Hector Mine, California, earthquake, estimated from satellite radar and GPS measurements. *Bull. Seismol. Soc. Am*. 92, 1377–1389. https://doi.org/10.1785/0120000922

Klimczak, C., 2014. Geomorphology of lunar grabens requires igneous dikes at depth. *Geology* 42, 963-966. H ttps://doi.org/10.1130/G35984.1

Koehn, D., Steiner, A., Aanyu, K., 2019. Modelling of extension and dyking-induced collapse faults and fissures in rifts. *J. Struct. Geol.* 118, 21–31. https://doi.org/10.1016/j.jsg.2018.09.017

Maccaferri, F., Acocella, V., Rivalta, E., 2015. How the differential load induced by normal fault scarps controls the distribution of monogenic volcanism. *Geophys. Res. Lett.*, 42, 7507–7512. https://doi.org/10.1002/2015GL065638

Malin, M.C., Bell, J.F., Cantor, B.A., Caplinger, M.A., Calvin, W.M., Clancy, R.T., Edgett, K.S., Edwards, L., Haberle, R.M., James, P.B., Lee, S.W., Ravine, M.A., Thomas, P.C., Wolff, M.J., 2007. Context Camera Investigation on board

the Mars Reconnaissance Orbiter. *J. Geophys. Res. E Planets* 112, 1–25. https://doi.org/10.1029/2006JE002808

Mandelbrot, B.B., 1982. The Fractal Geometry of Nature: San Francisco, W.H. Freeman and co., 468 p. https://doi.org/10.1002/esp.3290080415

Mazzarini, F., Armienti, P., 2001. Flank cones at Mount Etna volcano: do they have a power-law distribution? *Bull. Vocanol*., 62:420-430. https://doi.org/10.1007/s004450000109

Mazzarini, F., 2004. Volcanic vent self-similar clustering and crustal thickness in the northern Main Ethiopian Rift. *Geophysical Research Letters*, 31, L04604. https://doi.org/10.1029/2003GL018574

Mazzarini,F., Isola, I., 2010. Monogenetic vent self-similar clustering in extending continental crust: examples from the East African Rift System. *Geosphere*, 6, 567-582. https://doi.org/10.1130/GES00569.1

Mazzarini, F., Musumeci, G., Cruden, A.R., 2011. Vein development during folding in the upper brittle crust: The case of tourmaline-rich veins of eastern Elba Island, northern Tyrrhenian Sea, Italy. *Journal of Structural Geology*, 33, 10, 1509-1522. https://doi.org/10.1016/j.jsg.2011.07.001

McGovern, P.J., 2007. Flexural stresses beneath Hawaii: Implications for the October 15, 2006, earthquakes and magma ascent. *Geophys. Res. Lett*. 34, 1–6. https://doi.org/10.1029/2007GL031305

McGovern, P.J., Morgan, J.K., 2009. Volcanic spreading and lateral variations in the structure of Olympus Mons, Mars. *Geology* 37, 139–142. https://doi.org/10.1130/G25180A.1

McGovern, P.J., Grosfils, E.B., Galgana, G.A., Morgan, J.K., Rumpf, M.E., Smith, J.R., Zimbelman, J.R., 2015. Lithospheric flexure and volcano basal boundary conditions: Keys to the structural evolution of large volcanic edifices on the terrestrial planets. *Geol. Soc. Spec. Publ*. 401, 219–237. https://doi.org/10.1144/SP401.7

McKenzie, D., McKenzie, J.M., Saunders, R.S., 1992. Dike emplacement on Venus and on Earth. *J. Geophys. Res*. 97, 977–990. https://doi.org/10.1029/92je01559

Mège, D., Masson, P., 1996. A plume tectonics model for the Tharsis province, Mars. Planet. *Space Sci.* 44, 1499–1546. https://doi.org/10.1016/S0032-0633(96)00113-4

Mège, D., A. C. Cook, E. Garel, Y. Lagabrielle, and M.-H. Cormier, 2003. Volcanic rifting at Martian grabens, J. Geophys. Res.,108, 5044. https://doi.org/10.1029/2002JE001852

Melosh, H.J., Williams, C.A., 1989. Mechanics of graben formation in crustal rocks: A finite element analysis. *J. Geophys. Res*. 94, 13961– 13973. https://doi.org/10.1029/JB094iB10p13961

Meyzen, C.M., Massironi, M., Pozzobon, R., Zilio, L.D., 2014. Are terrestrial plumes from motionless plates analogues to Martian plumes feeding the giant shield volcanoes? *Geol. Soc. London, Spec. Publ*. 401, 107–126. https://doi.org/10.1144/SP401.8

Mohajeri, N., and Gudmundsson, A., 2012. Entropies and Scaling Exponents of Street and Fracture Networks. *Entropy*, 14, 800-833. https://doi.org/10.3390/e14040800

Montesi, L. G. J. 2001, Concentric dikes on the flanks of Pavonis Mons: Implications for the evolution of Martian shield volcanoes and mantle plumes, in Mantle Plumes: Their Identification Through Time, edited by R. E. Ernst and K. L. Buchan, *Spec. Pap. Geol. Soc. Am*., 352, 165–181. https://doi.org/10.1130/0-8137-2352-3.165

Montesi, L.G.J., Zuber, M.T., 2003. Clues to the lithospheric structure of Mars from wrinkle ridge sets and localization instability. *Journal of Geophysical Research*, 108, E6, 5048. https://doi.org/10.1029/2002JE001974

Moratto, Z., Broxton, M.J., Beyer, R.A., Lundy, M., Husmann, K., 2010. Ames Stereo Pipeline, NASA's Open Source Automated Stereogrammetry Software. *41st Lunar and Planetary Science Conference*, March 1-5, 2010, The Woodlands, Texas (USA). LPI Contribution No. 1533, p.2364.

Mueller, K., Golombek, M., 2004. Compressional structures on Mars. *Annual Rev. Earth. Planet. Sci.*, 32, 435–464. https://doi.org/10.1146/annurev.earth.32.101802.120553

Okada, Y., 1992. Internal deformation due to shear and tensile faults in a half-space. *Bull. Seismol. Soc. Am*. 82, 1018–1040.

Pagli, C., Mazzarini, F., Keir, D., Rivalta, E., Rooney, T.O., 2015. Introduction: Anatomy of rifting: Tectonics and magmatism in continental rifts, oceanic spreading centers, an transforms, *Geosphere*, 11(5), 1256-1261. https://doi.org/10.1130/GES01082.1

Plescia, J.B., 2004. Morphometric properties of Martian volcanoes. J. Geophys. Res. 109, E03003. https://doi.org/10.1029/2002JE002031

Plescia, J.B., 2000. Geology of the Uranius group volcanic constructs: Uranius Patera, Ceraunius Tholus, and Uranius Tholus. *Icarus* 143, 376–396. https://doi.org/10.1006/icar.1999.6259

Pozzobon, R., Mazzarini, F., Massironi, M., Pio, A., Pondrelli, M., Cremonese, G., Marinangeli, L., 2019. Fluids mobilization in Arabia Terra, Mars: Depth of pressurized reservoir from mounds self-similar clustering. *Icarus* 321, 1–22. https://doi.org/10.1016/j.icarus.2018.12.023

Pozzobon, R., Mazzarini, F., Massironi M., Marinangeli, L., 2015. Self-similar clustering distribution of structural features on Ascraeus Mons (Mars): implications for magma chamber depth. *Geological Society, London, Special Publications*, 401. https://dx.doi.org/10.1144/SP401.12

Reese, C.C., Solomatov, V.S., Baumgardner, J.R., Stegman, D.R., ezolainen, A. V., 2004. Magmatic evolution of impact-induced Martian mantle plumes and the origin of Tharsis. *J. Geophys. Res. E Planets* 109, 1–10. https://doi.org/10.1029/2003JE002222

Robbins S.J., Di Achille G., Hynek B.M., 2011. The volcanic history of Mars: High-resolution crater-based studies of the calderas of 20 volcanoes. *Icarus* 211 (2011) 1179–1203. https://doi.org/10.1016/j.icarus.2010.11.012

Ruiz, J., McGovern, P.J., Jiménez-Díaz, A., López, V., Williams, J.P., Hahn, B.C., Tejero, R., 2011. The thermal evolution of Mars as constrained by paleo-heat flows. *Icarus* 215, 508–517. https://doi.org/10.1016/j.icarus.2011.07.029

Shean, D.E., Head, J.W., Marchant, D.R., 2005. Origin and evolution of a cold-based tropical mountain glacier on Mars: The Pavonis Mons fan-shaped deposit. *Journal of Geophysical Research*, 110, E05001. https://doi.org/10.1029/2004JE002360

Schultz, R.A., 2000. Localization of bedding plane slip and backthrust faults above blind thrust faults: Keys to wrinkle ridge structure. Journal of Geophysical Research, 105, E5, 12035-12052. https://doi.org/10.1029/1999JE001212

Schultz, R.A., Okubo, C.H., Goudy, C.L., Wilkins, S.J., 2004. Igneous dikes on Mars revealed by Mars Orbiter Laser Altimeter topography. *Geology* 32, 889–892. https://doi.org/10.1130/G20548.1

Schultz, R.A., Soliva, R., Okubo, C.H., Mège D., 2010. Fault populations. In: Planetary Tectonics, edited by Thomas R. Watters and Richard A. Schultz. Cambridge University Press, Cambridge (UK), 457-510. https://doi.org/10.1017/CBO9780511691645.011

Scholz, C.H., Dawers, N.H. Yu, J.-Z., Anders, M.H., Cowie, P.A., 1993. Fault Growth and Fault Scaling Laws' Preliminary Results. *Journal of Geophysical Research*, 98, B12, 21951-21961. https://doi.org/10.1029/93JB01008

Scott, D.H., Tanaka K.L., 1986. Geologic map of the western equatorial region of Mars, U.S. *Geol. Surv. Misc. Invest. Ser.* Map, I-1802-A, scale 1:15,000,000. https://doi.org/10.3133/i1802A

Scott, D.H., Dohm, J.M., Zimbelman, J.R., 1998. Geologic map of Pavonis Mons volcano, Mars. U.S. Department of the Interior, U.S. Geological Survey, Atlas of Mars, 1:1,000,0000 Geologic Series Pavonis Mons Volcano, M 1M 2.5/115 G, 1998, I-2561

Smith, D.E., Zuber, M.T., Frey, H.V., Garvin, J.B., Head, J.W., Muhleman, D.O., Pettengill, G.H., Phillips, R.J., Solomon, S.C., Zwally, H.J., Banerdt, W.B., Duxbury, T.C., Golombek, M.P., Lemoine, F.G., Neumann, G.A., Rowlands, D.D., Aharonson, Oded, Ford, P.G., Ivanov, A.B., Johnson, C.L., McGovern, P.J., Abshire, J.B., Afzal, R.S., Sun, Xiaoli, 2001. Mars Orbiter Laser Altimeter—Experiment summary after the first year of global mapping of Mars. *Journal of Geophysical Research*, 106, E10, 23,689–23,722. https://doi.org/10.1029/2000JE001364

Soliva, R., and Schultz, R.A., 2008. Distributed and localized faulting in extensional settings: Insight from the North Ethiopian Rift–Afar transition area. *Tectonics*, 27, TC2003. https://doi.org/10.1029/2007TC002148

Tanaka, K. L., Robbins, S. J., Fortezzo, C. M., Skinner, J. A. & Hare, T. M., 2014. The digital global geologic map of Mars: Chronostratigraphic ages, topographic and crater morphologic characteristics, and updated resurfacing history. *Planet. Space Sci*. 95, 11–24. https://doi.org/10.1016/j.pss.2013.03.006

Torson, J.M., Becker, K.J., 1997. ISIS - A Software Architecture for Processing Planetary Images. *28th Annual Lunar and Planetary Science Conference*, March 17-21, 1997, Houston, Texas (USA). LPI Contribution No. 1219, p. 1443.

Tanaka, K.L., Skinner, J.A., Jr., Dohm, J.M., Irwin, R.P., III, Kolb, E.J., Fortezzo, C.M., Platz, T., Michael, G.G., and Hare, T.M., 2014, Geologic map of Mars: U.S. Geological Survey Scientific Investigations Map 3292, scale 1:20,000,000. https://dx.doi.org/10.3133/sim3292

Violay, M., Gibert, B., Mainprice, D., Evans, B., Dautria, J-M., Azais, P., Pezard, P., 2012. An experimental study of the brittle-ductile transition of basalt at oceanic crust pressure and temperature conditions. *Journal of Geophysical Research*, 117, B03213. https://doi.org/10.1029/2011JB008884

Voll, G., 1976. Recrystallization of quartz, biotite, and feldspars from Erstfeld to the Levantina nappe, Swiss Alps, and its geological implications. *Schweiz. Min. Petrol. Mitt.* 56, 641-647. http://doi.org/10.5169/seals-43709

Watts, A.B., 2001. Isostasy and Flexure of the Lithosphere. Cambridge University Press, Cambridge (UK), 458pp. Werner, S.C., 2009. The global martian volcanic evolutionary history. *Icarus* 201, 44–68. https://doi.org/10.1016/j.icarus.2008.12.019

Walsh, J.J., and Watterson, J., 1993. Fractal analysis of fracture pattern using the standard box-counting technique: Valid and invalid methodologies. *Journal of Structural Geology* 15, 1509–1512. https://doi.org/10.1016/0191-8141(93)90010-8

Watters, T., Robinson, M., Banks, M. et al., 2012. Recent extensional tectonics on the Moon revealed by the Lunar Reconnaissance Orbiter Camera. *Nature Geosci.* 5, 181–185. https://doi.org/10.1038/ngeo1387

Wilson, L., Head, J.W., 2002. Tharsis-radial graben systems as the surface manifestation of plume-related dike intrusion complexes: Models and implications. *J. Geophys. Res.*,107, E8, 5057. https://doi.org/10.1029/2001JE001593

Wilson, M.F.J., O'Connell, B., Brown, C., Guinan, J.C., Grehan, A.J., 2007. Multiscale Terrain Analysis of Multibeam Bathymetry Data for Habitat Mapping on the Continental Slope, *Marine Geodesy* 30, 3-35. https://doi.org/10.1080/01490410701295962

Wyrick, D.Y., Smart, K.J., 2009. Dike-induced deformation and Martian graben systems. *J. Volcanol. Geotherm. Res.* 185, 1–11. https://doi.org/10.1016/j.jvolgeores.2008.11.022

Yin, A., 2012. An episodic slab-rollback model for the origin of the Tharsis rise on Mars: Implications for initiation of local plate subduction and final unification of a kinematically linked global plate-tectonic network on Earth. *Lithosphere* 4, 553–593. https://doi.org/10.1130/L195.1

Zhong, S., 2008. Migration of Tharsis volcanism on Mars caused by differential rotation of the lithosphere. *Nat. Geosci.* 2, 19–23. https://doi.org/10.1038/ngeo392

Zimbelman, J.R., Edgett, K.S., 1992. The Tharsis Montes, Mars: comparison of volcanic and modified landforms. *Proceedings of Lunar and Planetary Science* 22, Houston, Texas (USA), March 18-22, 1991 (A92-30851 12-91), p. 31-44.

Zuber, M.T., 2000. Internal Structure and Early Thermal Evolution of Mars from Mars Global Surveyor Topography and Gravity. *Science* 287, 1788–1793. https://doi.org/10.1126/science.287.5459.1788

Figures

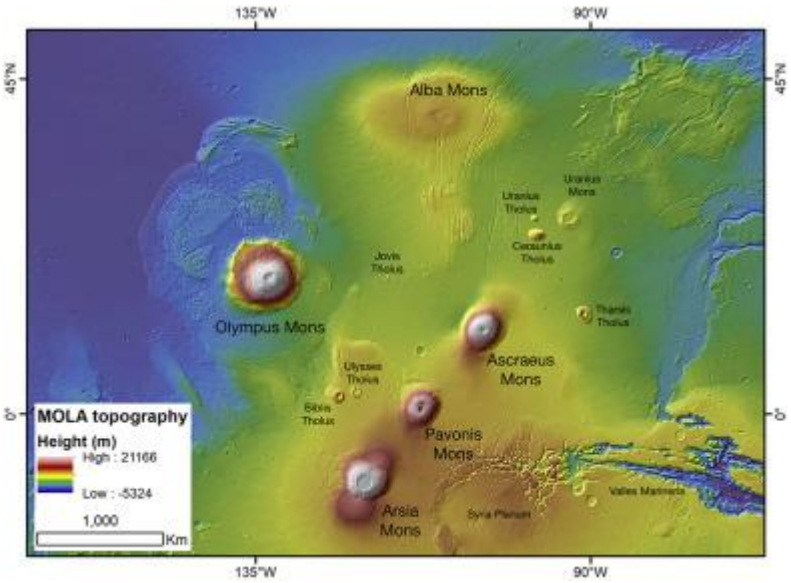

Figure 1

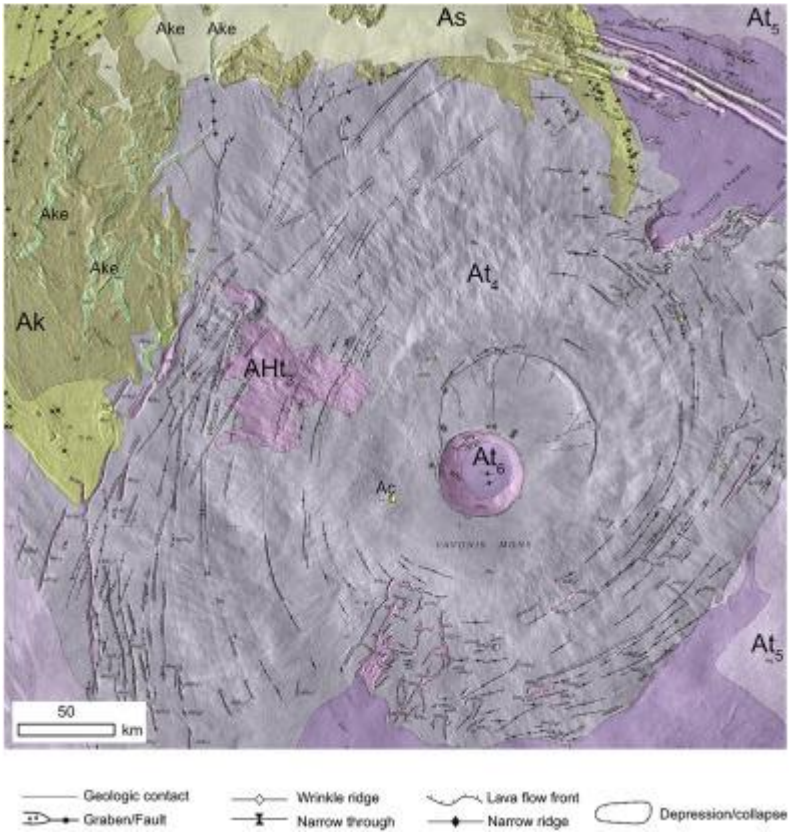

Figure 2

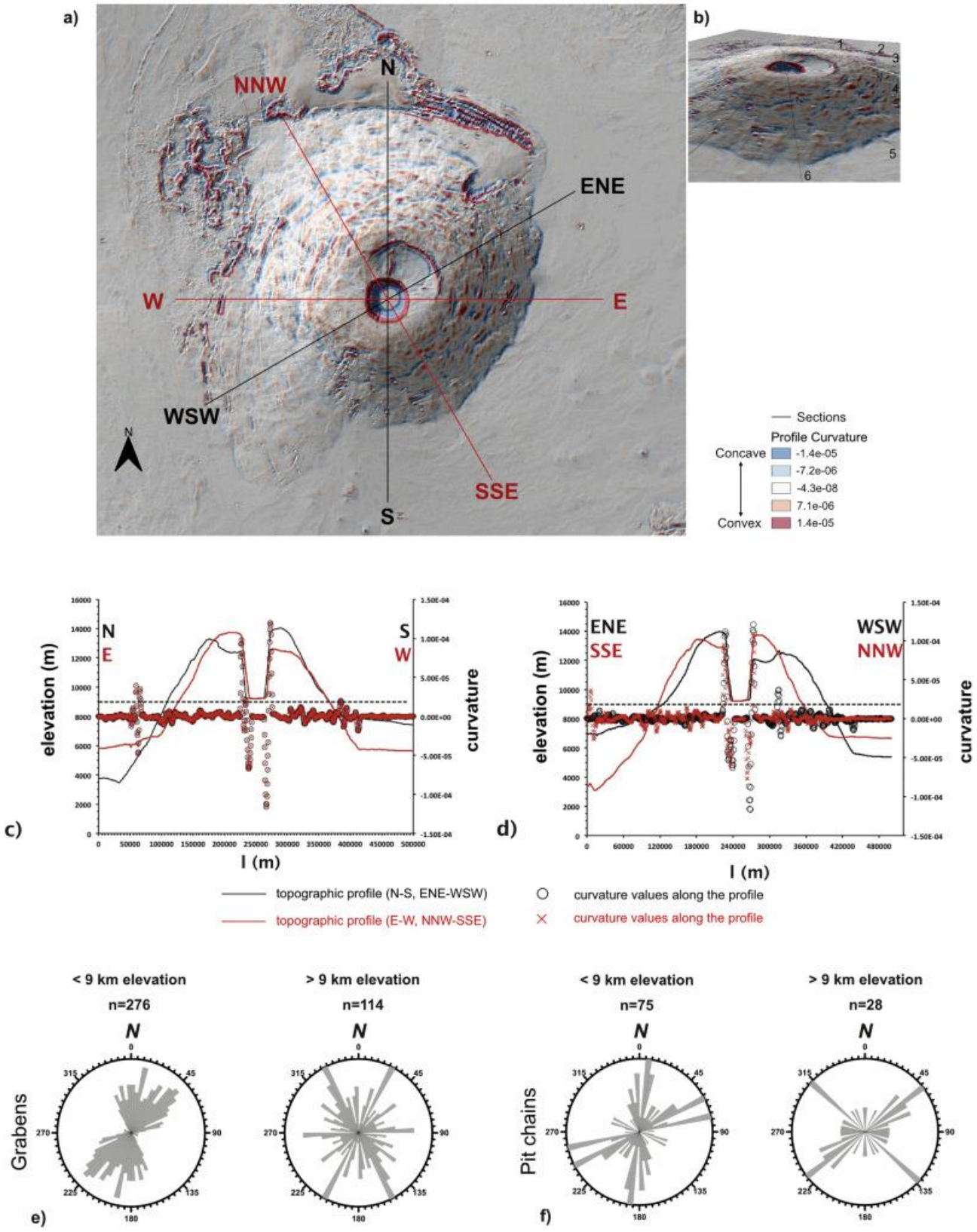
a)
b)
N
NNW
ENE
W
E
WSW
SSE
S
Sections
Profile Curvature
Concave
Convex
-1.4e-05
-7.2e-06
-4.3e-08
7.1e-06
1.4e-05
c)
d)
elevation (m)
curvature
l (m)
topographic profile (N-S, ENE-WSW)
topographic profile (E-W, NNW-SSE)
curvature values along the profile
curvature values along the profile
< 9 km elevation
n=276
> 9 km elevation
n=114
< 9 km elevation
n=75
> 9 km elevation
n=28
Grabens
Pit chains
e)
f)

Figure 3

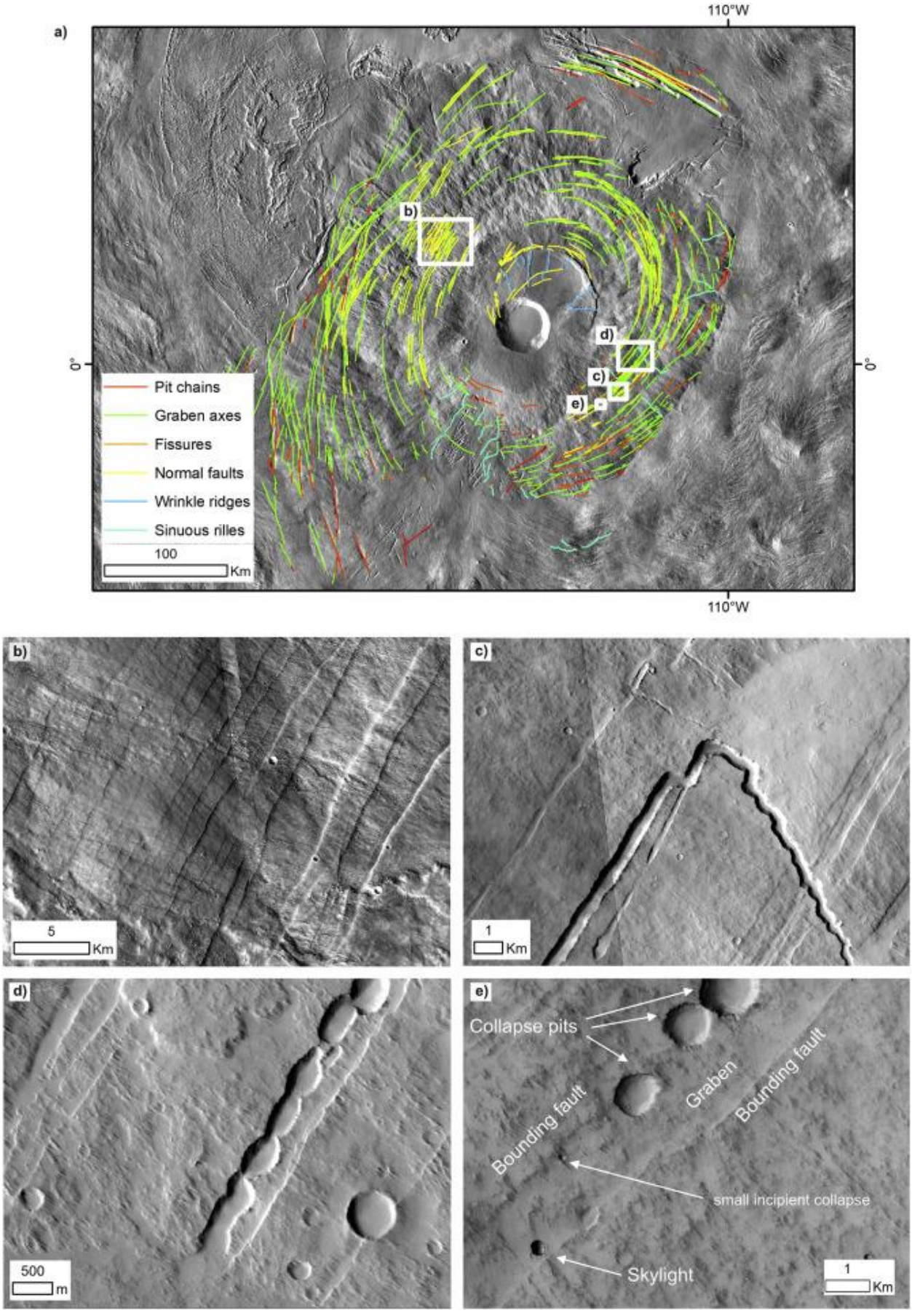
a)
110°W
0°
b)
d)
c)
e)
Pit chains
Graben axes
Fissures
Normal faults
Wrinkle ridges
Sinuous rilles
100
Km
b)
5
Km
c)
1
Km
d)
500
m
e)
Collapse pits
Bounding fault
Graben
Bounding fault
small incipient collapse
Skylight
1
Km

Figure 4

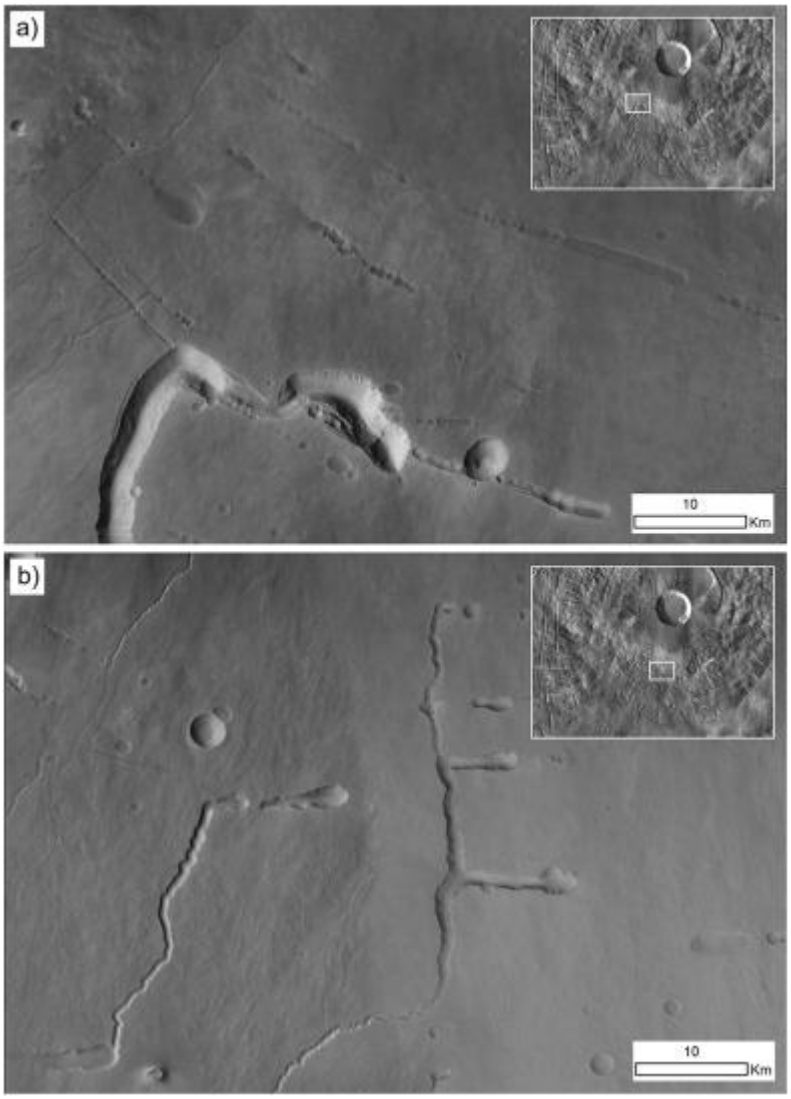

Figure 5

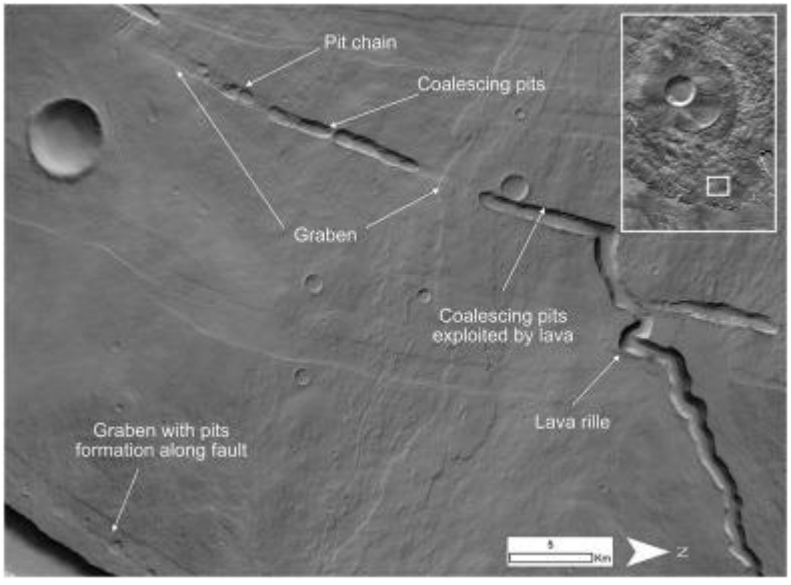

Figure 6

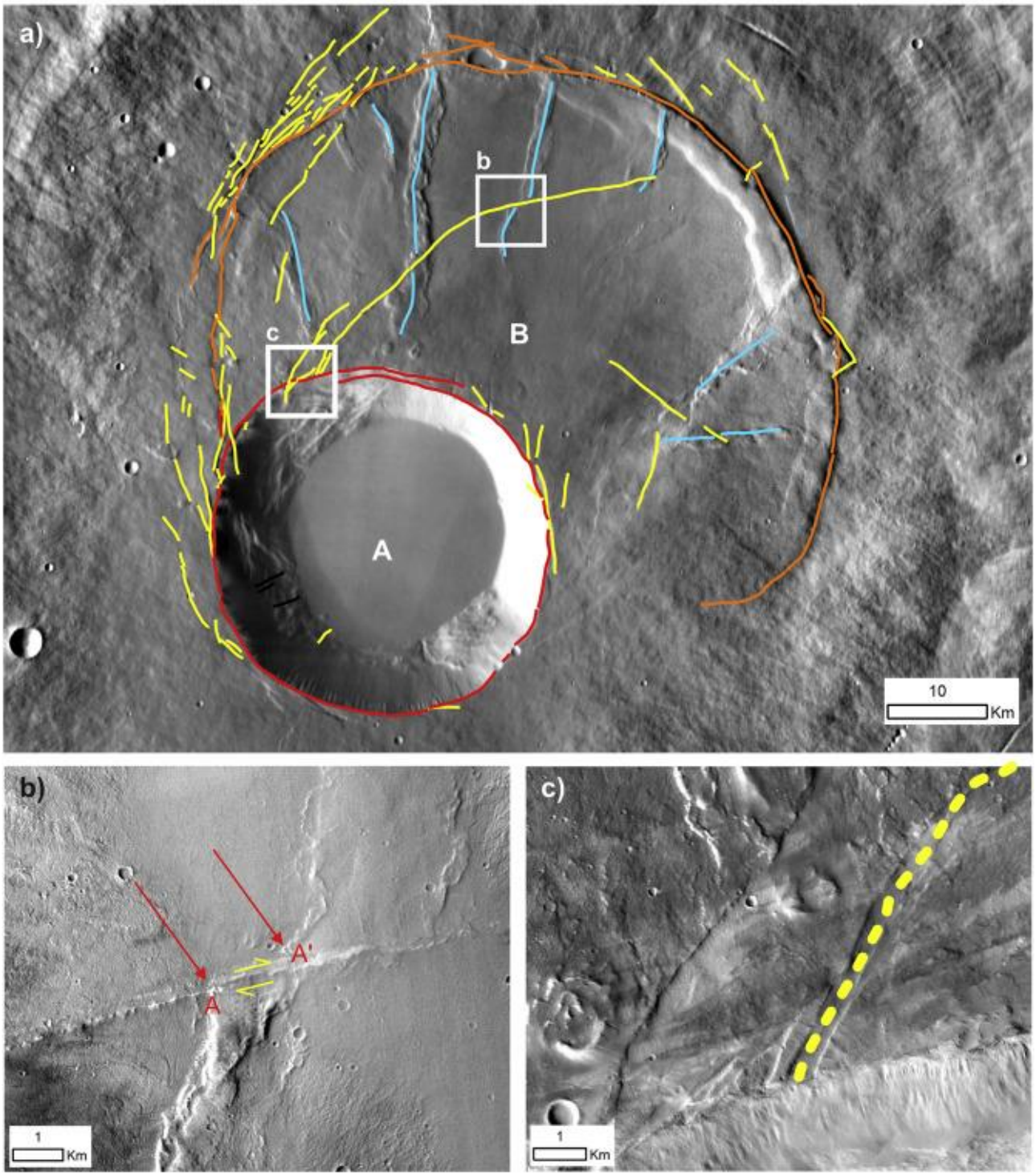

Figure 7

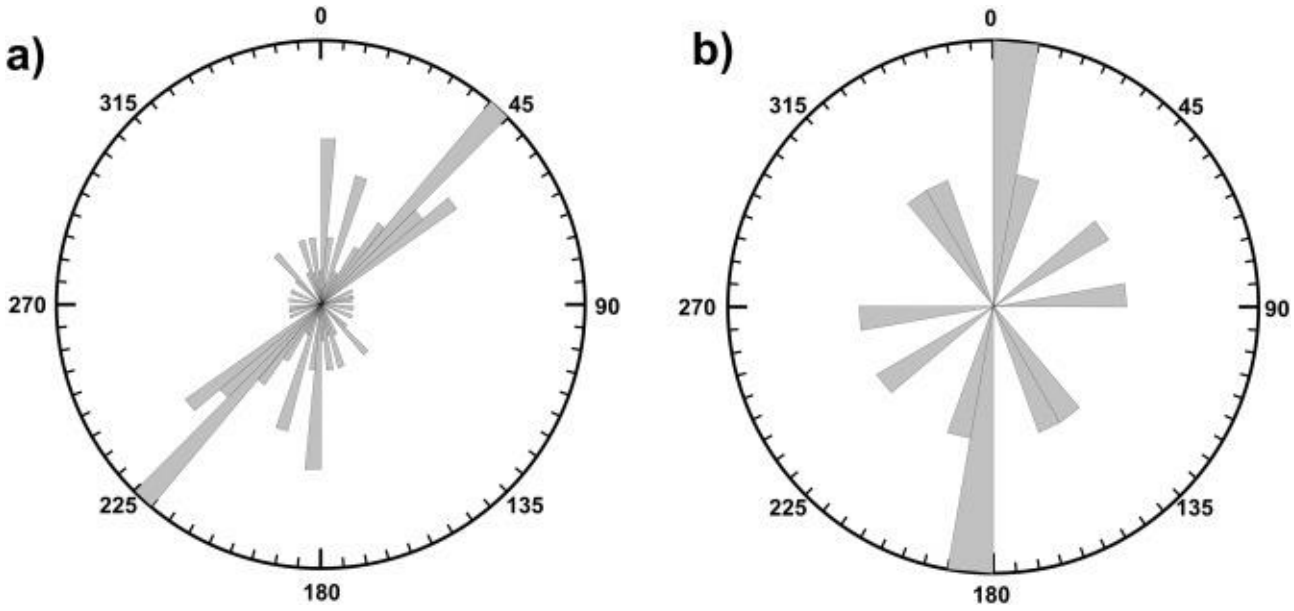

Figure 8

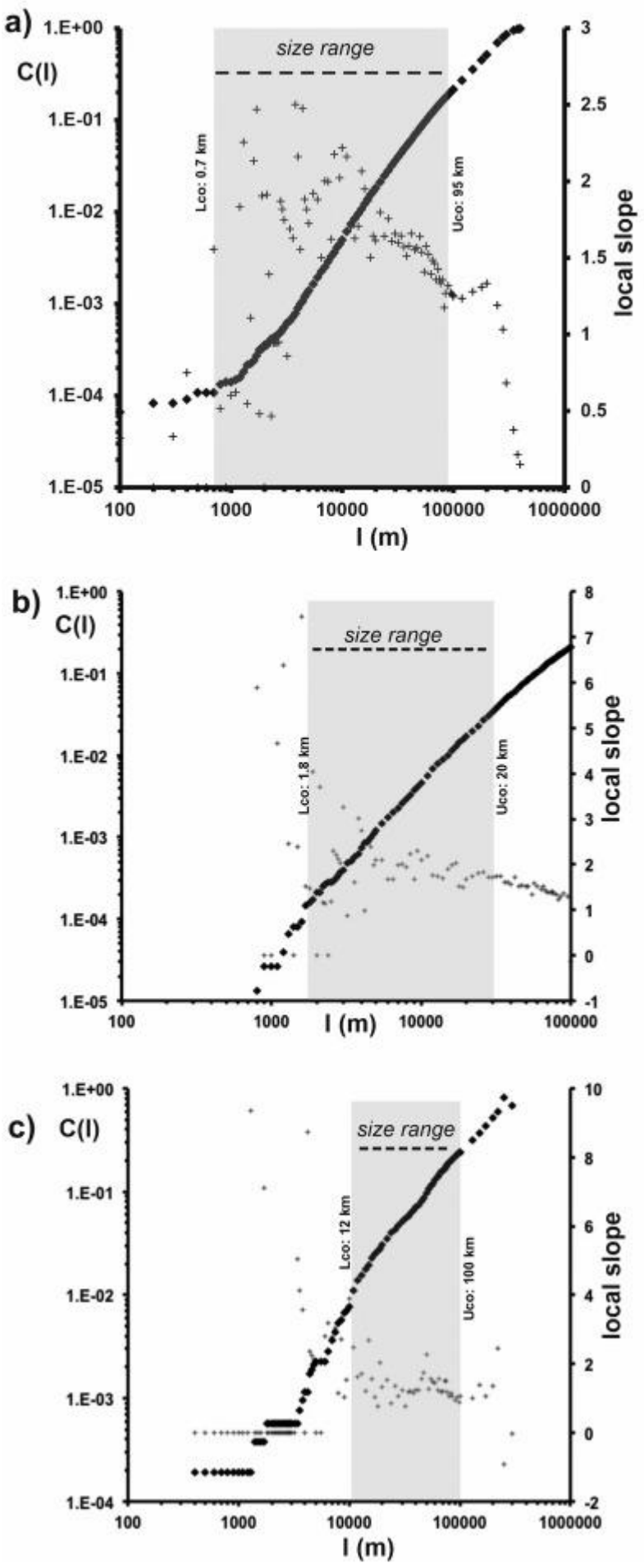
a)
C(l)
size range
Lco: 0.7 km
Uco: 95 km
local slope
l (m)
b)
C(l)
size range
Lco: 1.8 km
Uco: 20 km
local slope
l (m)
c)
C(l)
size range
Lco: 12 km
Uco: 100 km
local slope
l (m)

Figure 9

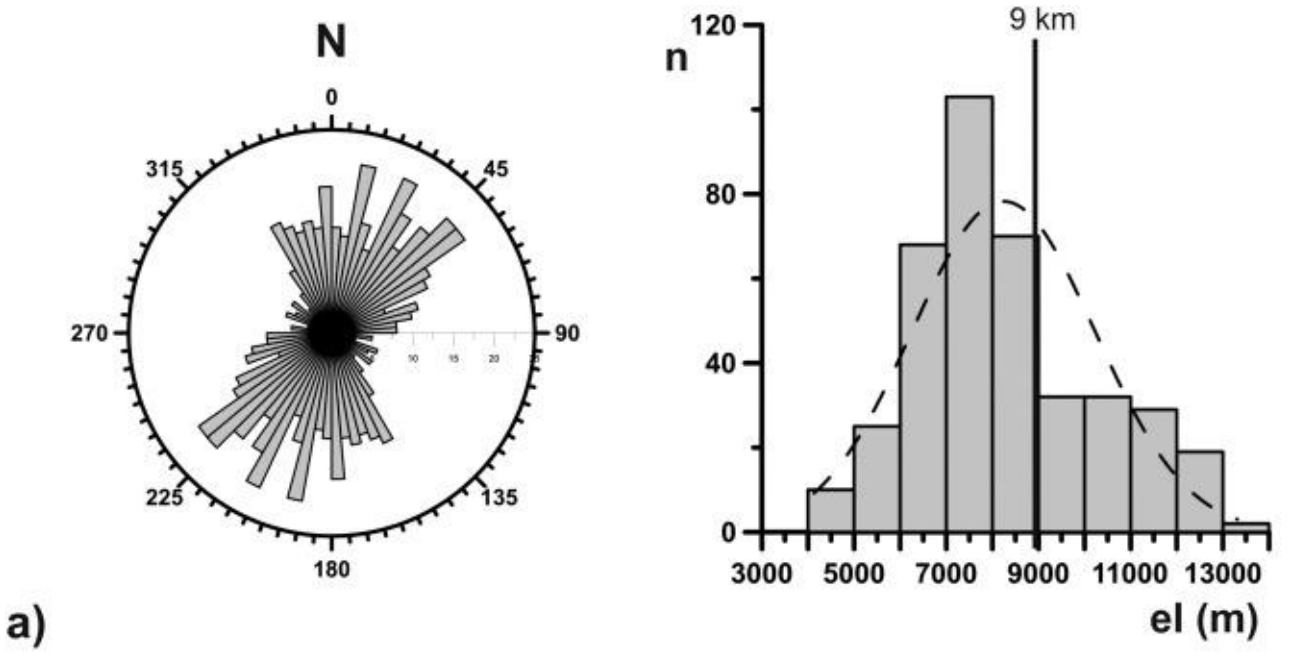
N
0
45
90
135
180
225
270
315
n
120
80
40
0
9 km
3000
5000
7000
9000
11000
13000
el (m)

a)

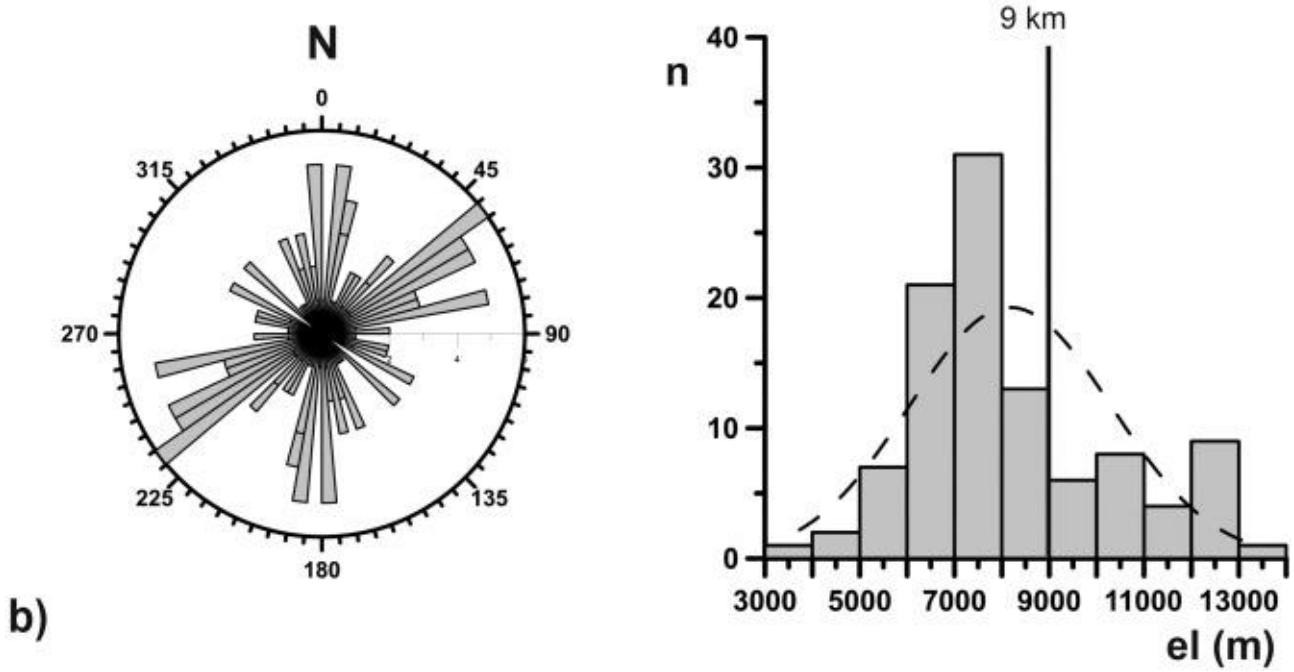
N
0
45
90
135
180
225
270
315
n
40
30
20
10
0
9 km
3000
5000
7000
9000
11000
13000
el (m)

b)

Figure 10

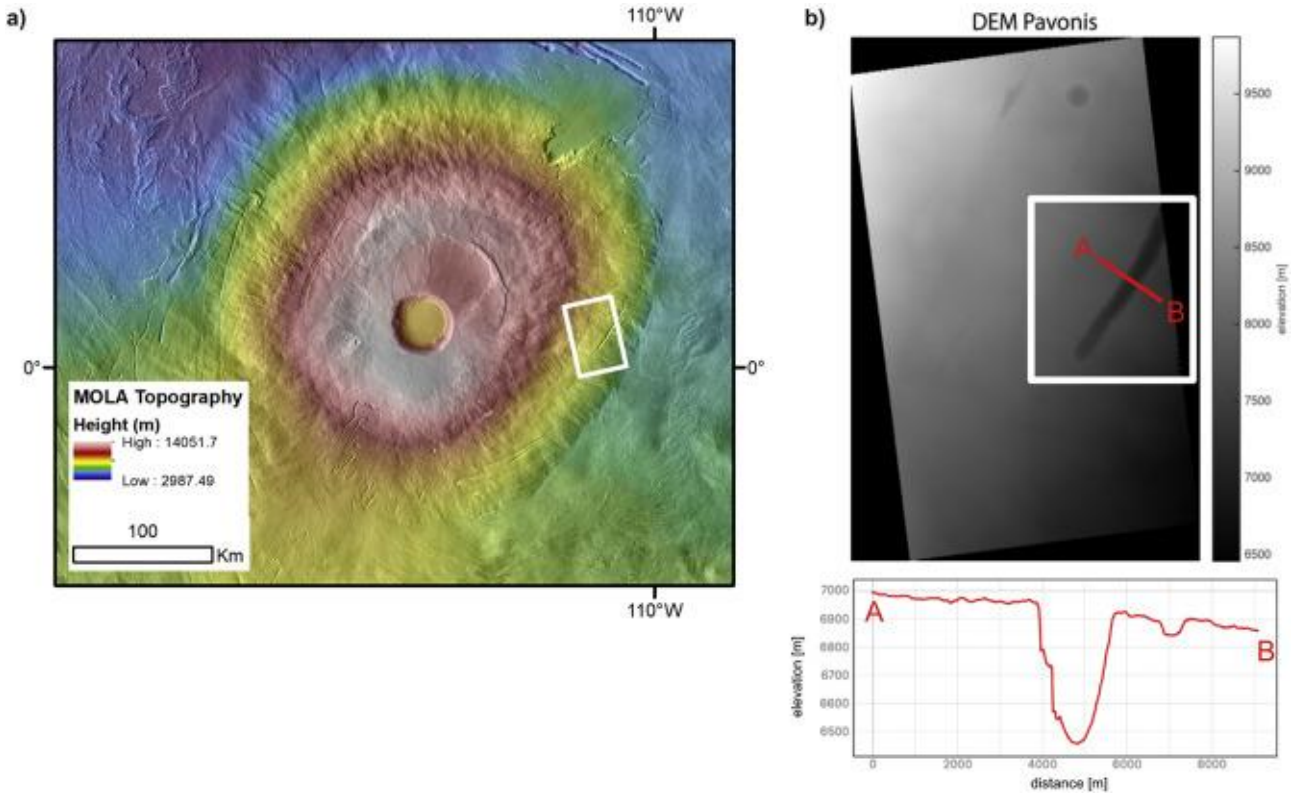
a)
110°W
0°
0°
110°W
MOLA Topography
Height (m)
High : 14051.7
Low : 2987.49
100
Km
b)
DEM Pavonis
A
B
9500
9000
8500
8000
7500
7000
6500
elevation [m]
7000
6900
6800
6700
6600
6500
elevation [m]
A
B
0
2000
4000
6000
8000
distance [m]

Figure 11

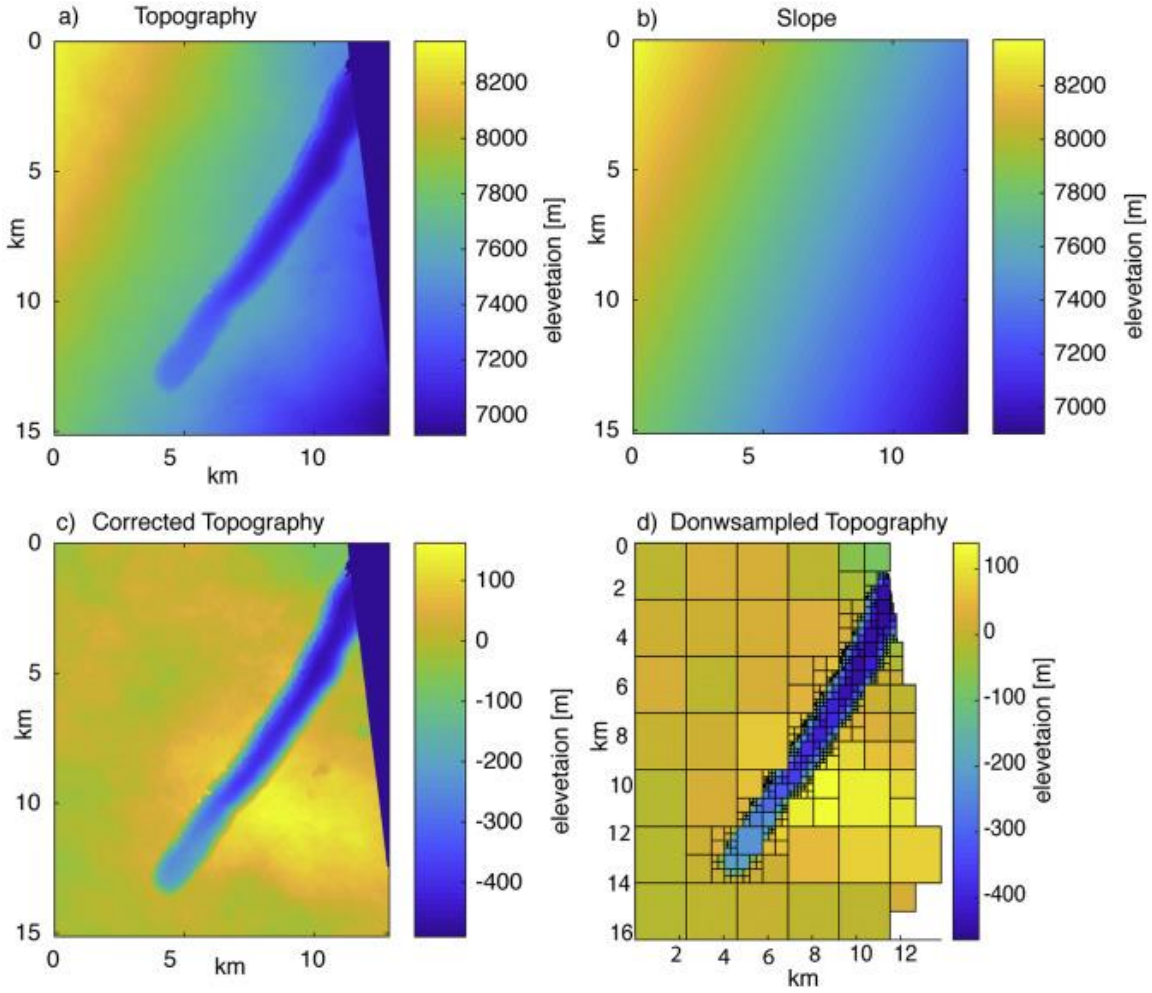
a) Topography
b) Slope
c) Corrected Topography
d) Donwsampled Topography
km
elevetaion [m]
8200
8000
7800
7600
7400
7200
7000
100
0
-100
-200
-300
-400

Figure 12

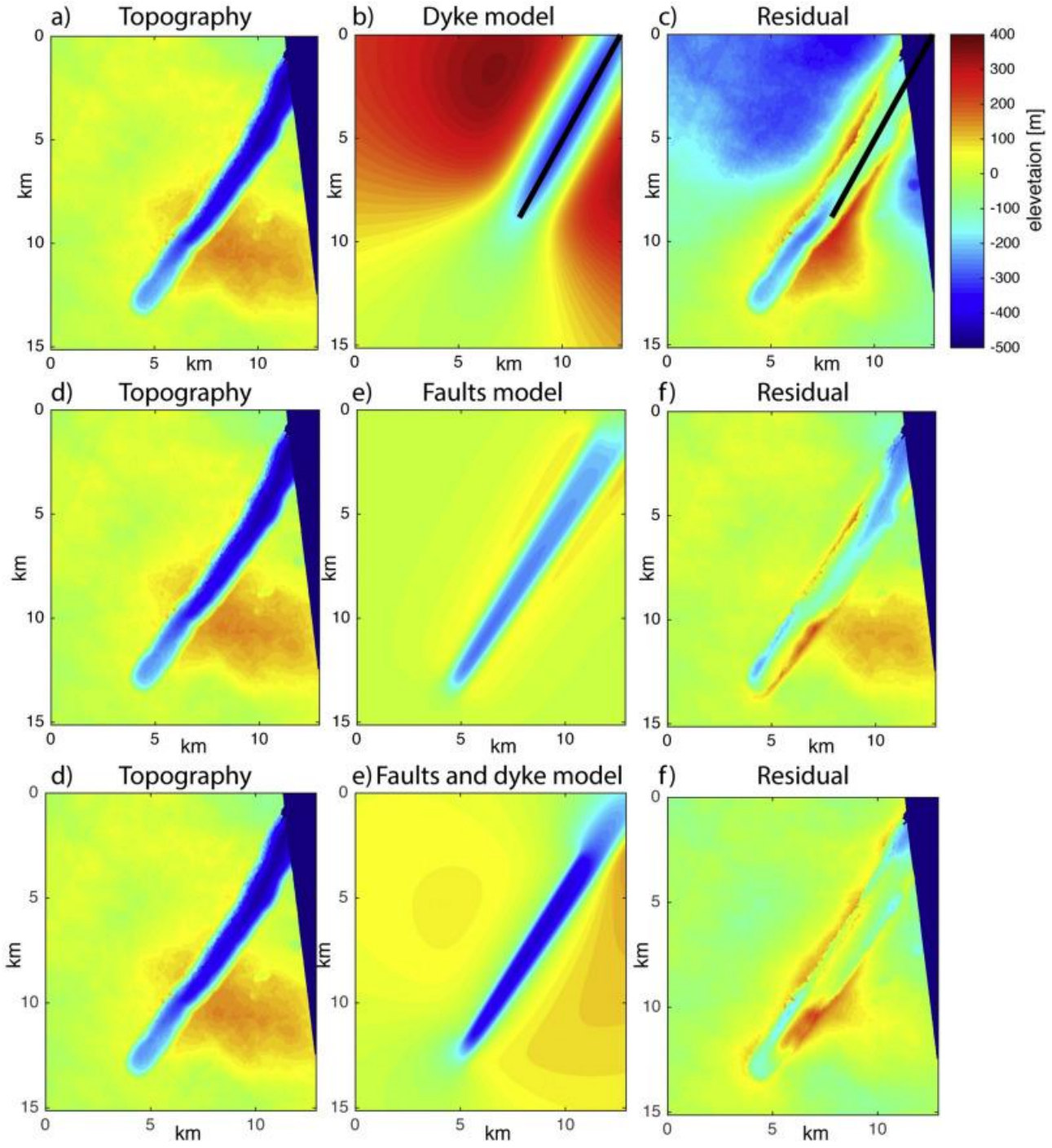
a) Topography
b) Dyke model
c) Residual
d) Topography
e) Faults model
f) Residual
d) Topography
e) Faults and dyke model
f) Residual
km
elevetaion [m]
400
300
200
100
0
-100
-200
-300
-400
-500

Figure 13

Tables

CTX product IDs	Ground resolution (m/pixel)	Phase angle	Incidence angle	Convergence angle	Expected vertical precision (m)	Coordinates of centroid
P04_002750_1819_XI_01N111W	5.08	58.65°	55.67°	11.5°	5.2	1.85 N 249.00 E
D17_033935_1803_XN_00N110W	5.15	37.72°	44.96°			0.32 N 249.22 E

Table 1

Data set	N	Distr.	s.r (km)	β, c	λ, a	R^2	$Lmax_{th}$ (km)	$Lmax_{obs}$ (km)	$\|\Delta Lmax\|$ (km)
all	493	n.e	0.7-132	476.05	$4x10^{-5}$	0.9895	154.1	132.6	21.5
Grabens	390	n.e	2.3-132	383.82	$4x10^{-5}$	0.9922	148.8	132.6	16.2
Pit chains	103	p.l.	6.5-55	10^{-s}	1.5910	0.9842	106.7	105.7	1

N: number of elements; Distr.: distributions; n.e.: negative exponential distribution; p.l.: power-law distribution; s.r.: size range; β,c: normalization constant in the negative exponential and power-law distribution, respectively; λ,a: exponential and fractal exponents, respectively; $Lmax_{th}$: maximum theoretic length; R^2: correlation factor; $Lmax_{obs}$: maximum observed length; $|\Delta Lmax|$: absolute value of the difference $Lmax_{th}$ - $Lmax_{obs}$.

Table 2

Data set	N	Lco (km)	Uco (km)	c	D	R^2
all	493	0.7 ± 0.4	95 ± 3.5	1×10^{-9}	1.6736	0.9960
Grabens	390	1.8 ± 0.2	20 ± 2.5	6×10^{-11}	1.9764	0.9991
Pit chains	103	12.0 ± 1.4	100.0 ± 8.5	5×10^{-8}	1.3330	0.9979

N: number of elements; Lco: lower cutoff; Uco: upper cutoff; c: normalization constant; D: fractal exponent; R2: correlation factor.

Table 3